NORTHWESTERN UNIVERSITY

Properties of a Graphene-based Nanocomposite and Nanopaper

A DISSERTATION

SUBMITTED TO THE GRADUATE SCHOOL IN PARTIAL
FULFILLMENT OF THE REQUIREMENT

for the degree

DOCTOR OF PHILOSOPHY

Field of Physics

by

Geoffrey H. B. Dommett

EVANSTON, ILLINOIS

December 2007

Abstract

Graphene sheets (one-atom-thick, two-dimensional layers of sp^2-bonded carbon) are predicted to have a range of unusual properties. Recent studies have shown that individual graphene sheets have extraordinary electrical properties, but finding an efficient method of graphite exfoliation remains a challenge. A number of approaches to exfoliation have been tried, such as rubbing graphite or using adhesive tape to separate the layers, but these methods are unlikely ever to provide sufficient quantities of material for applications.

In this work, two potential applications of graphene-based sheets have been investigated, namely nanocomposites, and graphene-based paper. Electrical measurements were made on the nanocomposites to elucidate their electrical properties. Since it was necessary to take measurements on teraohm impedances at low temperatures down to 10K, a custom cryostat insert with exceptionally low leakage current had to be designed and fabricated. This is described.

Composite materials were prepared by using a solution-based chemical approach, exfoliating graphite oxide into individual, chemically-modified graphene sheets embedded in a polystyrene matrix. Composites prepared by the solution-based approach were found to be electrically conductive even when using very small amounts of graphene-based filler; reaching a room-temperature conductivity of $10^{-6}Sm^{-1}$ with a graphene-based sheet concentration of 0.15%, the lowest concentration that was measured. The conductivity of the composite was found to depend not only on the concentration of graphene-based filler in the composite, but also on the

mechanical and thermal history of the material, which could render the composite completely insulating.

It has been shown that conduction within the composite takes place by a variable range hopping mechanism; and the dependence of the conductivity on the processing of the material is most likely due to the morphology of the polymer in which the graphene-based sheets are embedded.

Acknowledgements

I would especially like thank my advisor Professor Rodney Ruoff for all his support, and the summer student Cyrus Zalian-Rahatabad for his help with many aspects of this project, and t.

I would like to thank all other past and present students and postdoctors of the Ruoff group for their support during this project, Kevin Kohlhaas, Eric Zimney, Dr. Sasha Stankovich Dr Richard Piner and Dr. Dmitriy Dikin.

I would like to thank Professor Kenneth R Shull for valuable discussions concerning the properties of polymers, Robert Taglia for teaching me many of the skills needed to fabricate many parts made during this work, Byron Watkins, Stephen Jacobson for discussions about cryostat construction, and Neil Dilley at Quantum Design for discussions about how to interface with the PPMS system.

I would also like to thank my parents for their support throughout, and also for their help proofreading.

Table of Contents

Abstract 3

Acknowledgements 5

Table of Contents 6

Table of Figures 8

List of Tables 11

1. Introduction 12

2. Experimental setup 15

  2.1. Molding of composite material 15

    2.1.1. Injection molding 15

    2.1.2. Design of an injection molder for small samples 16

  2.2. Electrical configuration of transport measurements. 18

    2.2.1. Electronic equipment used for transport measurements 18

    2.2.2. Calculating resistivity from resistance data 21

  2.3. Low temperature measurements using the PPMS 24

  2.4. Taking low temperature data on high resistance samples 28

    2.4.1. Electrical guarding 29

    2.4.2. A custom insert for the PPMS 30

    2.4.3. Performance of the custom insert for the PPMS 36

    2.4.4. Recording electrical data 41

3. Graphene-based nanocomposite materials. 43

  3.1. Fabrication of a graphene-based nano-composite in a polystyrene matrix 45

  3.2. Conduction Mechanisms that are commonly applied to carbon polymer composites 48

3.2.1. Thermally activated tunneling ... 49

3.2.2. Mott Variable Range Hopping (VRH) ... 51

3.2.3. Efros-Shklovskii Variable Range Hopping (ES-VRH) ... 54

3.3. Electrical properties of a graphene-based nano-composite in a polystyrene matrix ... 55

3.3.1. Dispersion of the platelets within the composite ... 56

3.3.2. Qualitative Electrical properties ... 57

3.3.3. Time-dependent electrical properties of injection molded nano-composites at elevated temperature ... 59

3.3.4. Temperature dependent properties of the composite ... 63

3.3.5. Annealing of insulating samples ... 66

3.3.6. Activation energy of annealing ... 72

4. Graphene-oxide Paper ... 74

4.1. Chemical Properties of Graphene Paper ... 74

4.2. Chemical modification of Graphene-based paper ... 76

4.2.1. X-Ray Analysis of Graphene Based Paper ... 77

5. Summary and Future Work ... 81

References ... 83

Table of Figures

Figure 2.1 The custom molder. (a) top half, (b) piston, (c) bottom half, (d) securing plate. ..17

Figure 2.2 Electrical configuration of electrometers and typical sample dimensions. 6115's are electrometers configured to measure voltage and 6415 is a current source. All 3 devices are unavoidably grounded internally. 20

Figure 2.3 Electrical potential and current distribution for a typical sample, 1mm thick, electrodes 2mm wide with a gap of 0.5mm between the electrodes......................22

Figure 2.4 measured voltage V1 and V2 using the connections internal to the cryostat on a 4% composite sample kept at (a) 17K, measured resistance is 190GΩ, (b) 11K, measured resistance is 50GΩ (c) 5K, measured resistance is 11GΩ (d), 2K, measured resistance is 11GΩ The electrometers were connected using the wiring internal to the cryostat. The current sourced was (a) 2hr at 50pA 2hr, 2hr at –50pA, 2hr at –100pA (b) 7hr at 50pA 7hr at -50pA, (c) 5hr at 50pA 10hr at -50pA, (d) 4hr at 50pA, 6hr at -50pA. 26

Figure 2.5 I-V data for 1% injection molded composite sample at 130K and 30K, recorded using the insert described in section 2.4.2. 27

Figure 2.6 Resistance against temperature for a 4% weight composite sample measured in the quantum design PPMS using electrometers connected to the sample using the wiring internal to the cryostat. 28

Figure 2.7 The flange for the insert that sits at the top of the cryostat..................................31

Figure 2.8 The custom insert for the cryostat that provides guarding of all signals. 33

Figure 2.9 Spacers between the stainless steel tubes. (a) inner teflon spacers used from the top of the cold zone to the top of the cryostat (b) inner boron nitride spacers used in the cold zone, (c) outer teflon spacers used from the cold zone to the top of the cryostat. Pennies are present for scale. 35

Figure 2.10 measured voltage V1 and V2 using the connections internal to the cryostat on a 4% composite sample kept at (a) 17K, programmed source current ±3.56pA, measured impedance 1.2TΩ (b) 16K, programmed source current ±1.74pA, measured impedance 2.5TΩ (c) 15K, programmed source current ±854fA measured impedance 5.7TΩ (d) 13K, programmed source current ±59.8fA measured impedance 19TΩ 38

Figure 2.11 Resistance versus temperature for a 4% weight composite sample measured in the quantum design PPMS using the custom insert. 40

Figure 2.12 The pucks that the samples sit on (a) the supplied puck by quantum design that connects to the cabling internal to the cryostat, (b) the circuit board that the sample sits in for mounting using the custom insert. 41

Figure 3.1 Atomic force microscopy of a dried down suspension of exfoliated graphite oxide that has been exfoliated by ultrasonication. 44

Figure 3.2 Atomic force microscopy of a dried down suspension of exfoliated graphite oxide that has been exfoliated by stirring. 45

Figure 3.3 Nano- composite powder that has been fabricated by the solution based approach (a) before vacuum drying when it is a grey powder, (b) after drying when it is black, coagulated and electrically conductive. 46

Figure 3.4 Process for the entire fabrication process of making the graphene-based nanocomposite. 47

Figure 3.5 SEM of a fracture surface of hot pressed 1% weight chemically modified graphene sheets in in polystyrene. 56

Figure 3.6 SEM images of fracture surface of composite containing 0.5% weight of chemically modified graphene sheets in polystyrene that was prepared by injection molding and then annealed; higher magnification images obtained in the indicated regions. 57

Figure 3.7 Resistance of molded 5%wt CREGO in polystyrene sample as it is annealed. During the time that the temperature is kept constant at 247°C, the resistance increases slightly 61

Figure 3.8 Resistance vs time as composite samples are annealed 62

Figure 3.9 Resistivity versus $T^{-1/2}$ for both injection molded and hot pressed samples. Pressed = Hot Pressed, IM = Injection Molded, an. = time that the sample was annealed at 180°C. Best fit straight lines are also shown. 66

Figure 3.10 Room temperature resistivity versus weight percent filler concentration for the composite materials. 68

Figure 3.11 Resistance versus time as composite samples are annealed. 71

Figure 3.12 Arrhenius plots of the rate constants for the annealing of 0.5 % weight and 0.75% weight grapheene based filler composite materials. 73

Figure 4.1 X-Ray diffraction patterns of pristine and amine-treated samples of graphene oxide paper (left). Dependence of the d-spacing on the alkyl chain length (right).78

Figure 4.2 SEM images of the fracture surface of a ~10 mm-thick graphene oxide paper sample before and after treatment with dodecylamine. 80

List of Tables

Table 3.1 Variable range hopping parameters for the composites..65

Table 3.2 Rate constants for the annealing of the composite samples..70

1. Introduction

Graphene sheets (one-atom thick, two-dimensional layers of sp^2-bonded carbon) are predicted to have a range of unusual properties. Recent studies have shown that individual graphene sheets have extraordinary electrical properties[1-5]; but an efficient method of graphite exfoliation remains a challenge. A number of approaches to exfoliation have been tried, such as rubbing graphite or using adhesive tape to separate the layers, but these methods are unlikely ever to provide sufficient quantities of material for applications.

Within my group we have developed a method for exfoliating bulk graphite via a solution process. Although this method requires large amounts of solvents, it is capable of processing much more material than surface techniques; furthermore, the solvents could be recovered and re-circulated -a benefit for any future industrial setting which might require the production of large amounts of material. In this work, I have looked at two potential applications of graphene: nanocomposite materials and graphene paper.

Composite materials were prepared by using a chemical approach, exfoliating graphite oxide into individual, chemically-modified graphene sheets embedded in a polystyrene matrix. Composites prepared by our solution-based approach were found to be electrically conductive even when using very small amounts of graphene-based filler; reaching a room temperature conductivity of $10^{-6}Sm^{-1}$ with a graphene-based sheet concentration of 0.15%, the lowest concentration that was measured. The conductivity of the composite was found to depend not only on the concentration of graphene-based filler in the composite, but also on the mechanical and thermal history of the material, which could render the composite completely insulating.

To be able to utilize these composites, it is essential to understand how the above-mentioned factors affect the composite's conductivity. Temperature-dependent measurements of the composite's resistivity were made to elucidate the mechanism by which the conduction took place. Thermal and mechanical processing of the composite strongly affected its electrical properties. These dependencies have been characterized, but details of the mechanisms by which processing affects the electrical properties are beyond the scope of this work.

Inorganic “paper-like” materials based on nanoscale components such as exfoliated vermiculite or mica platelets have been intensively studied and commercialized as protective coatings, high temperature binders, dielectric barriers, and gas-impermeable membranes. Carbon-based flexible graphite foils composed of stacked platelets of expanded graphite, have long been used in packing and gasketing applications due to their chemical resistivity against most media, superior sealability over a wide temperature range, and impermeability to fluids. The discovery of carbon nanotubes brought about bucky paper, which displays excellent mechanical and electrical properties that make it potentially suitable for fuel cell and structural composite applications, for example.

Chapter 2 describes the experimental setup that was used. To characterize the composites fully required solving several technical challenges. Developing the ability to measure resistances of several teraohms at low temperature required the fabrication of special equipment and is a major accomplishment of this work. Equipment was also constructed to replicate industrial processing conditions of laboratory-size samples of composite materials. Experimental results and an introduction to relevant theory concerning charge transport on the composite materials are presented in chapter 3. Experimental results on the intercolation of graphene paper with amines are detailed in chapter 4

The chapters are written so as to be as self-contained at possible so that they can be read in any order. Extensive cross referencing is provided throughout to that the reader wishing to read the chapters out of order should be able to do so.

2. Experimental setup

In this chapter the experimental techniques and fabricated equipment used to measure the composite samples will be described. Techniques were developed to injection mold samples with only 3 grams of polymer, and for the measurement of samples at low temperature with resistances of many teraohms.

2.1. Molding of composite material

The first composite samples fabricated were prepared by hot pressing - a commonly used method for lab preparation of polymers- but this process was not reliably repeatable. Sometimes hot-pressed samples would have significant bubbles in them, rendering them completely useless. A better method of fabricating samples was necessary.

2.1.1. Injection molding

Injection molding is one of the most common ways of forming thermo-melting plastics into parts. It was desired to prepare these composite samples by injection molding, first to improve the reliable repeatability of their preparation, and second, to see if the composite was affected in any way by this method of preparation. An injection molding machine was available to us, but like most commercial injection molders, it would have required us to fabricate at least fifty pounds of material just to fill the screw so that the machine would operate. This was an impossible quantity to prepare using the solution-based chemistry, for reasons which are discussed in section 3.1. A custom molder was therefore fabricated that would replicate industrial molding conditions as closely as possible, and enable us to do a single mold shot with just three grams of composite powder.

Injection molding, as its name suggests, consists of forcing polymer through a gate (a small hole) at high speed into a cavity that is the shape of the molded part. The size of the hole is usually quite small so that the finished part breaks off at the gate as easily as possible. The temperature is typically kept as low as possible: firstly, so that the formed part solidifies in the cavity as fast as possible; and secondly, to minimize thermal degradation of the plastic. The speed at which the molding process can be repeated is very important in an industrial setting. On a commercial molder, the plastic must also be cool enough for it not to flow out of the injection nozzle under the force of gravity. The pressure of injection is typically several hundred psi, as the polymer is very viscous at the temperature of operation.

2.1.2. Design of an injection molder for small samples

The approach taken for the laboratory molder was simple. It consisted of two halves that were bolted together (see Figure 2.1a and c). A piston was used to pressurize the composite, Figure 2.1b, and a plate to bolt the mold together, Figure 2.1d. The top and bottom halves of the mold had cavities to form the samples, with gates onto the central hole in which the composite was initially placed. The walls of the cavity were tapered 2 degrees to facilitate the release of the fabricated samples from the mold. Vents were present to allow escape of air from the cavities.

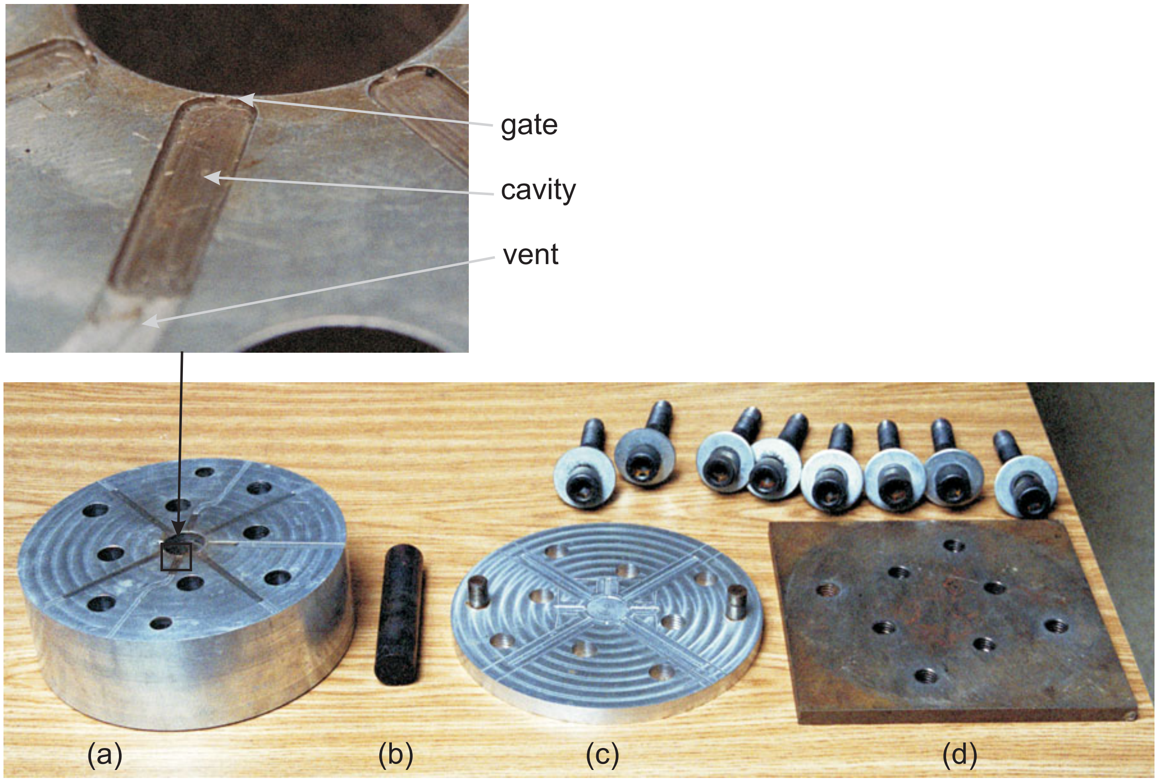

Figure 2.1 The custom molder. (a) top half, (b) piston, (c) bottom half, (d) securing plate.

To perform a fabrication run, the mold was bolted together, coated with Sprayon™ polystyrene mold release, and heated using a hot plate. The temperature was measured using a thermometer inserted in a hole in the block. Once the mold had reached 140˚C, the composite material was inserted into the central hole, and the piston inserted. The mold was then transferred to a hydraulic press and the piston depressed. It was then transferred from the press and immersed in water to cool it down. The polymer would have spent approximately 10 minutes at a temperature above 100˚C. Whilst this cooling process was significantly slower than in industrial injection molding, where the plastic would be heated and the mold held at a lower temperature, these processing conditions were the closest approximation to injection molding that could be achieved with the limited quantities of composite material available.

As will be described later, injection molding as a method of sample preparation did have dramatic effects on the composite material, reducing the electrical conductivity in excess of 10 orders of magnitude. It is presumed that this is due to the high shear flow that the material was subjected to during the injection process.

2.2. Electrical configuration of transport measurements.

The aim of these transport measurements was to measure the bulk properties of the composite materials. The graphene-based nanofiller sheets in the composite had lateral dimensions as big as a micron. To ensure that bulk properties were being measured, dimensions of test samples had to be much greater than the largest dimensions of the sheets(~1μm). This necessitated ensuring that the smallest dimension of the samples or the electrodes attached to the samples was no less than a few hundred microns in size. Since the geometry of the available cryostat allowed the largest dimensions of the samples to be no greater than 1cm, and the resistance increased rapidly as temperature decreased, to measure these composite samples, it was necessary to perform transport measurements on very high resistances. Typical sample dimensions are shown in Figure 2.2.

2.2.1. Electronic equipment used for transport measurements

Concerning the electrical transport data of the composite materials, it was necessary to be able to measure impedances of several teraohms as the impedance of these materials increased dramatically as the temperature was reduced. Standard multi-meters in the lab could be switched to an input impedance of no more than 10GΩ. Preliminary measurements on the composites indicated that the mechanism of electrical conduction was most likely to be a variable range hopping model. However, to be sure of this, it was necessary to measure the resistivity over as large a temperature range as possible. Initially we tried to measure these samples using a Keithley 6430 electrometer, which has the capability to carry out four-wire measurements and has an input impedance of $10^{16}\Omega$. This did not work because although the electrometer has a very high input impedance, it cannot tolerate having a large voltage drop between the sense and the source without giving an erroneous measurement. Four wire measurements taken using the 6430 did not match four wire measurements taken using other equipment. It was verified using a network of known resistors that the four wire resistance measurement mode of the 6430 was not suitable for this application. Electrical measurements were taken using two Keithley 6514 electrometers with input impedances of 100 TΩ and a Keithley 6115 current source with an output impedance of 200TΩ connected together as shown in Figure 2.2. This is a configuration that was recommended by Keithley, and since it was the best configuration that could be assembled for the price, was used for all electrical transport measurements. The only improvement possible would have been using three 6430's, but this would have cost in excess of $25 000. It may seem that the second electrometer was unnecessary and instead one electrometer could have been connected across the outside pair of electrodes. To have done this would have resulted in a three-wire measurement giving erroneous resistance data. A single electrometer only has one high-impedance input and a ground. It was essential that only one electrode on the sample was connected to ground, or the sample would have been be shorted out leading to an erroneous measurement. Since the current source was connected across electrodes 2 and 3 in Figure 2.2, the electrometer could not be connected across electrodes 1 and 4, because to do so would have created a short between electrodes 3 and 4. Instead, two electrometers had to be used, and their readings subtracted.

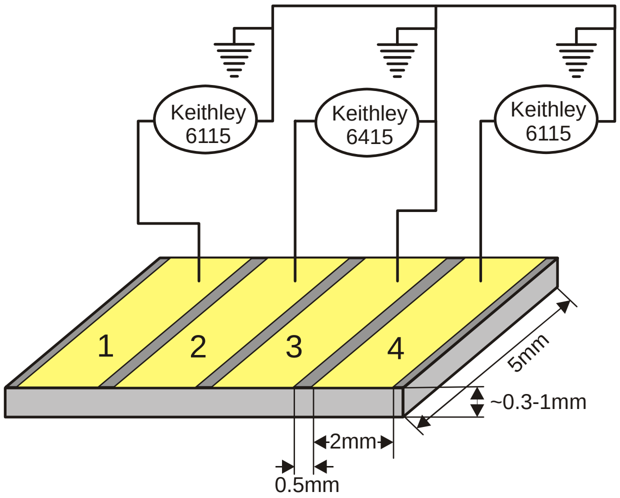

Figure 2.2 Electrical configuration of electrometers and typical sample dimensions. 6115's are electrometers configured to measure voltage and 6415 is a current source. All 3 devices are unavoidably grounded internally.

The reciprocity principle states that for a network of linear resistors an electromotive force (emf) in one branch of the network will produce the same current in the other branches as an equivalent circuit where the emf has been moved to another branch[6,7]. Thus for a linear system (the *I*-*V* dependence of the sample and interface is linear), the electrode arrangement in Figure 2.2 is equivalent to the reverse configuration ($R_{23}^{14} = R_{14}^{23}$) where the outer electrodes are the current terminals and the inner electrodes measure potential. The proof of this principle for the general case of any arbitrary geometry or network of resistors may be found elsewhere[6]. The proof was also verified using the finite element model discussed in section 2.2.2 that although the current distribution in the sample is different for R_{23}^{14} and R_{14}^{23}, both configurations will have the same resistance for a given interface resistance and material resistivity.

Although these two configurations (R_{23}^{14} and R_{14}^{23}) will give identical data, the reverse configuration to that shown in Figure 2.2, although in some ways more conventional, would have had the current sourcing through a resistance that was at least twice as large. Since the sample resistances were very large at low temperature, it was desired not to make them any bigger than they needed to be. Accordingly, all electrical data presented in this thesis was measured using the configuration shown in Figure 2.2.

2.2.2. Calculating resistivity from resistance data

The geometry of the samples was chosen to make the resistance as low as possible, whilst still maintaining a meaningful measurement. The electrodes were 2mm wide with a gap of 0.5mm between them. This chosen geometry had the effect that the current distribution, far from remaining uniform within the test sample, varied throughout the sample, as shown in Figure 2.3. In this regime, simply taking the distance between the electrodes and dividing it by the cross section of the sample would have given an erroneous resistivity, off by a factor of between 2 and 10 depending on the resistance on the interface between the electrodes and the sample. A finite element model using Comsol Multiphysics™ was therefore developed[8] to calculate the resistivity of a sample from resistance data.

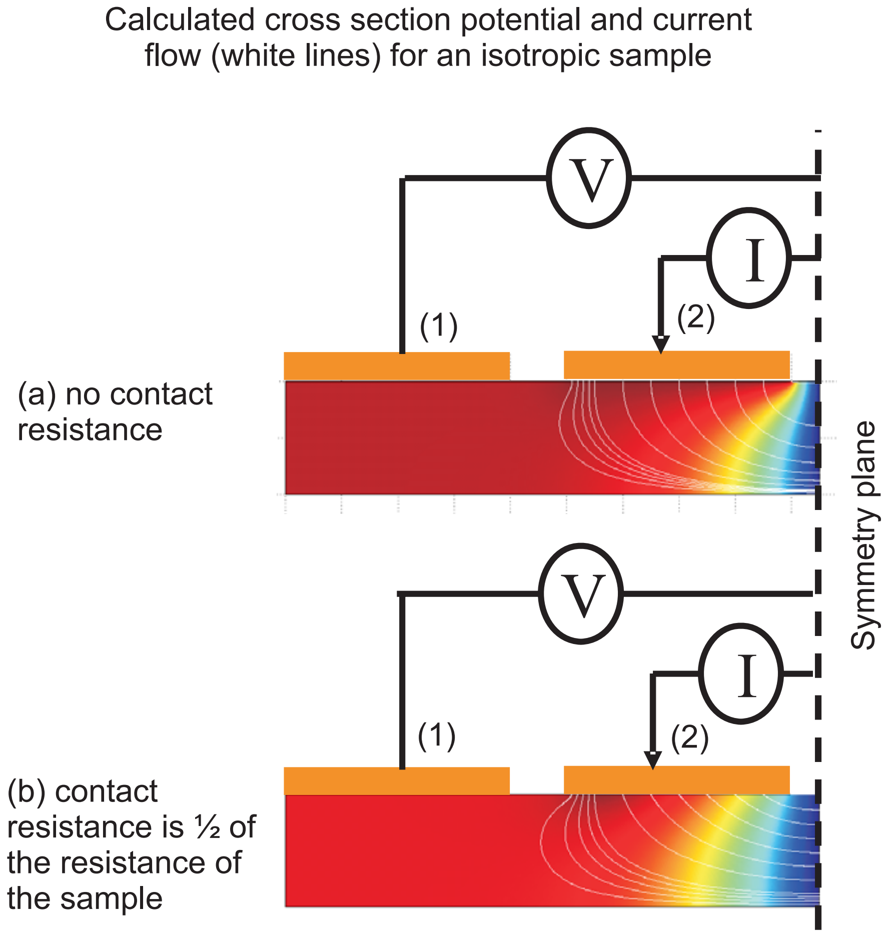

Figure 2.3 Electrical potential and current distribution for a typical sample, 1mm thick, electrodes 2mm wide with a gap of 0.5mm between the electrodes.

Using the finite element model it was possible to calculate the potential at (1) and (2) for a given source current, sample resistivity and interface resistance. There was however the problem that increasing the interface resistance affected the current distribution in the sample, as can be seen from the difference between Figure 2.3a and Figure 2.3b. The four-wire resistance measurement was not completely independent of interface resistance, as would have been in the case had the electrodes been infinitely small. Instead, the interface resistance could affect the four-wire resistance measurement by up to a factor of 2, for a given sample resistance as discussed elsewhere[8]. Since the interface resistance was not known, there were two parameters (resistivity and interface resistance) that had to be solved (it is impossible to calculate one without the other), so it was not possible to calculate a straight conversion factor between the resistance and the resistivity, and the model needed to be applied iteratively.

To calculate the resistivity of a sample, the finite element model was used inside a Matlab® program. The voltages at (1) and (2) were calculated for a known current and initial guesses as to sample resistivity and electrode interface resistance. A Newton Raphson method was then used to minimize the error of the voltages at (1) and (2) with respect to their measured values by varying the resistivity and interface resistance.

The down side of using a sample geometry with a non-uniform current distribution was that the finite element model was only valid in the regime where the resistance was linear. As with many materials, the resistance of the composite turned out to be linear so long as the applied voltage was not too high. For the geometry of the composite samples under test, the limit of applied potential was about 10 volts as can be seen from Figure 2.6. I-V data in the non-linear range cannot be considered reliable with this geometry. There was the added complication with I-V data, that it was not known how much of the observed non-linear effects were due to sample heating, and how much due to the resistivity of the material being non-linear. It should be kept in mind that even though the power dissipated in a high resistance material is small, the thermal conductivity of most polymers is very poor.

One approach to eliminating Joule heating from the measured data is to apply the current in pulses[9]. If the pulse length is short enough, it is possible to take an electrical resistance measurement before the test sample heats up significantly. A typical test for choosing an appropriate pulse length is to ensure that measurements are not significantly different when measured using two pulse lengths that differ by a factor of two. To measure the composite samples using this method would have been extremely difficult with such high impedances, where settling times of the electronics become significant, and was considered beyond the scope of this work. For this reason, the limitation of keeping the applied current in the linear range was not considered a problem. For all measurements presented in this thesis, data was taken at double the applied current as well as the current used to take the measurement, to check that the recorded data was in the linear range.

2.3. Low temperature measurements using the PPMS

The cryostat available for the measurements was a Quantum Design PPMS. This system has built-in resistance measurement capability, but it is designed to measure a maximum impedance of 4MΩ. The first thing that was tried was to disconnect the measurement electronics internal to the PPMS and connect the electrometers to the cabling internal to the cryostat that is supposed to go to the sample under test. The sample then sat on the standard PPMS electrical measurement puck. The data was taken by sourcing current and continuously measuring the voltage from the two electrometers, proceeding to the next measurement when the voltage readings had stabilized. This did work to a degree, but had some problems. The method worked at temperatures where the impedances were not too great. Above 30K, readings of V1 and V2 could be taken after waiting for a minute or two. However, as the temperature decreased, the resistance of the samples increased, which in turn caused stray capacitances and leakage currents to become more problematic. The recorded voltages as a function of time for selected temperatures are shown in Figure 2.4. At 17K, the measured voltage took in excess of an hour to stabilize, Figure 2.4c. As the temperature was reduced further, the measurement became more unstable Figure 2.4b-d. In Figure 2.4, the recorded voltage from the electrometers detailed in Figure 2.2 is shown as a function of time as the current is switched from positive to negative. The change in the settling time and final stability of the recorded voltages can be seen. The currents that were sourced for each plot shown in Figure 2.4 are shown in the caption. I-V plots for a 1% composite sample measured using the insert described in section 2.4.2 are shown in Figure 2.5. It can be seen that the resistance of the samples becomes more non-linear as temperature is decreased, but still remains fairly linear so long as the applied voltage is kept below about 10 Volts. For all data points presented in this thesis, linearity was checked visually for 4 data points, measuring positive and negative currents to eliminate any DC offset issues with the electrometers. Full I-V curves were not recorded at all temperatures, but measurements were also taken at double the current of the measurement to check that the measurement was taken in a linear range of the sample.

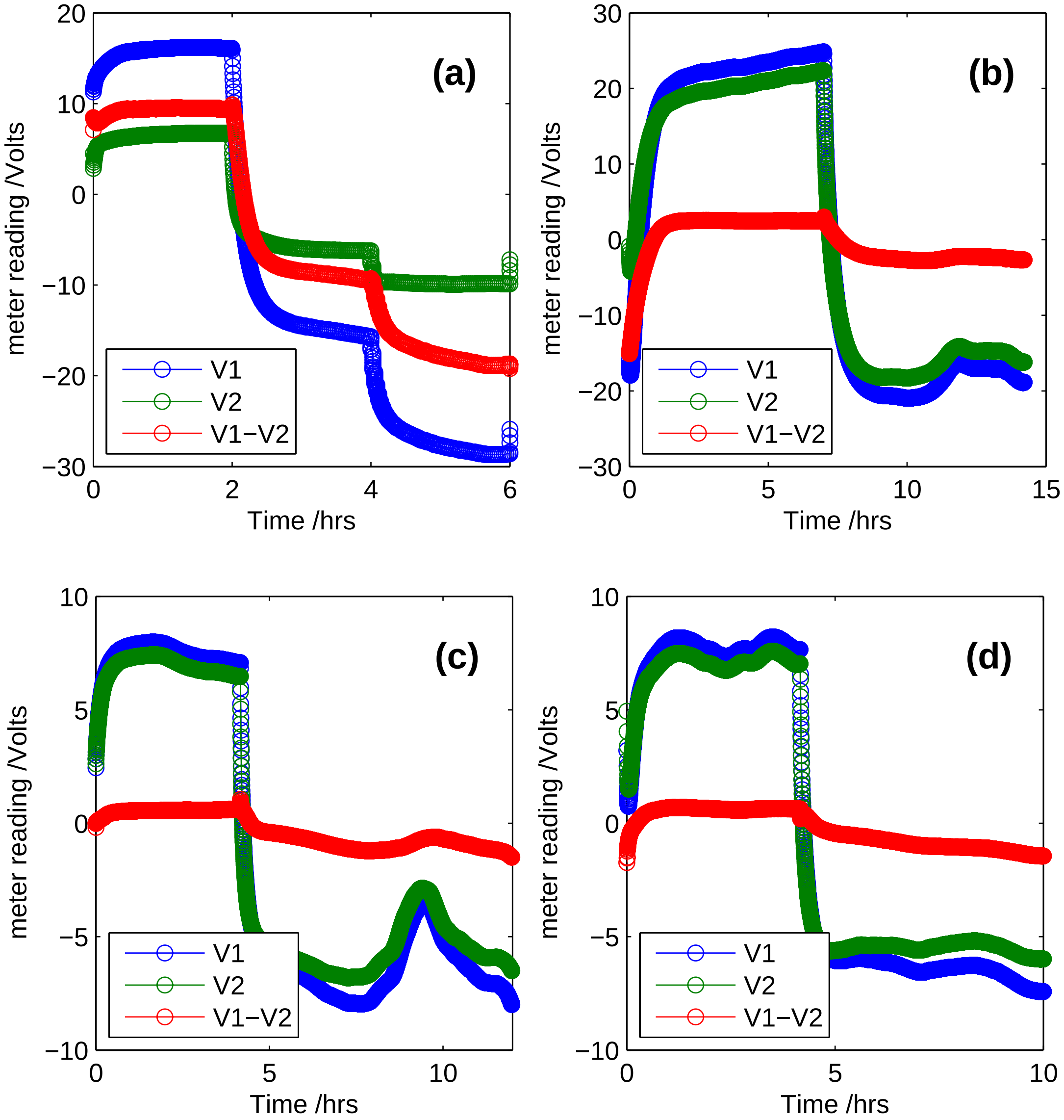

Figure 2.4 measured voltage V1 and V2 using the connections internal to the cryostat on a 4% composite sample kept at (a) 17K, measured resistance is 190GΩ, (b) 11K, measured resistance is 50GΩ (c) 5K, measured resistance is 11GΩ (d), 2K, measured resistance is 11GΩ The electrometers were connected using the wiring internal to the cryostat. The current sourced was (a) 2hr at 50pA 2hr, 2hr at –50pA, 2hr at –100pA (b) 7hr at 50pA 7hr at -50pA, (c) 5hr at 50pA 10hr at -50pA, (d) 4hr at 50pA, 6hr at -50pA.

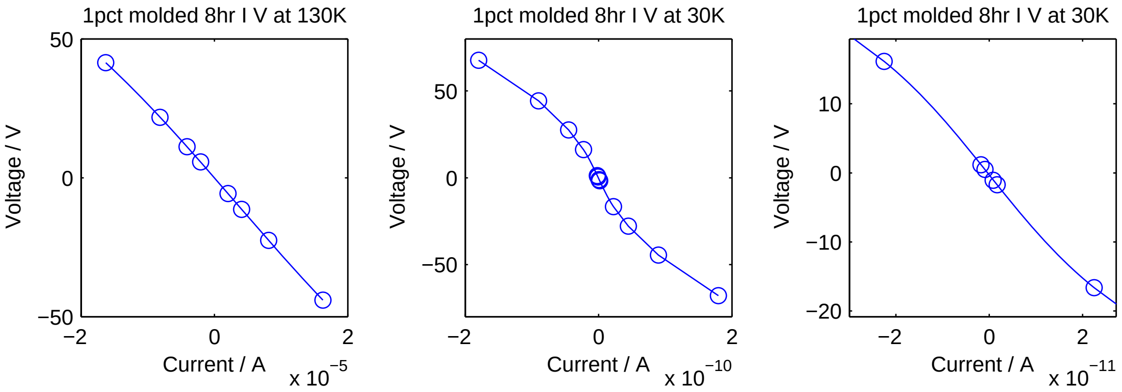

Figure 2.5 I-V data for 1% injection molded composite sample at 130K and 30K, recorded using the insert described in section 2.4.2.

The measured resistance versus temperature curve in the same sample is shown in Figure 2.6. It would appear from this that the resistance of the sample reached a maximum at around 17K before dropping off as temperature was decreased further, and that the interface resistance (defined by the voltage drop across electrodes 3 and 4 in Figure 2.2 divided by the source current) increased faster than the sample impedance as temperature decreased. It can be seen from Figure 2.4 that there were effects present that did not remain the same when the current through the sample was reversed. Since the sample was uniform, it seemed unlikely that this could have come from the sample, making the measured resistance data unreliable. These effects, as will later be shown, were measurement artifacts.

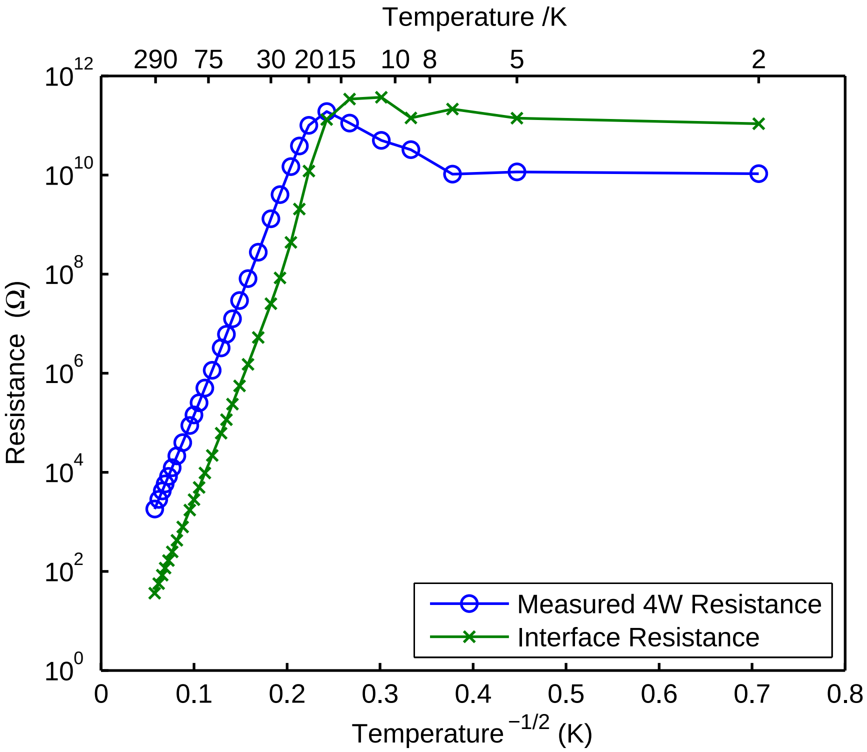

Figure 2.6 Resistance against temperature for a 4% weight composite sample measured in the quantum design PPMS using electrometers connected to the sample using the wiring internal to the cryostat.

2.4. Taking low temperature data on high resistance samples

The low temperature data taken by connecting the electrometers to the wiring that is internal to the cryostat was very slow to record. The plot shown in Figure 2.6 took five days to record. The time taken to do many samples this way would have been significant, and the cost of the required helium would have been immense.

The wiring built into the cryostat for making electrical measurements has an unknown parasitic capacitance and resistance. Since it was designed for use with samples with resistances that are 6 orders of magnitude less than the composite samples that were under test, it is unlikely that the designers of the cryostat would have felt any need to pay attention to these issues. To get reliable measurements, it was necessary to eliminate the possibility that the measured effects could be resultant from the wiring in the cryostat. The reliability of the data was questionable as well as being unacceptably slow, so a better method of taking data was required.

2.4.1. Electrical guarding

The 6514 electrometers in use have guarded inputs, and the current source has a guarded output, using triaxial connectors. A triaxial connector is shown in Figure 2.7. The principal of a guarded cable is that the signal should be encased in a shield that is kept at the same potential as the signal that is being guarded. In this configuration there is no potential across the insulation that is surrounding the signal, so all leakage current should be eliminated. In addition, parasitic capacitances between the signal and ground should be eliminated. When laying out traces on circuit boards, all signal traces should be surrounded by a guard trace so that there is nowhere for current to go across the surface of the circuit board, as nothing is going to stay perfectly clean forever. Modern chip design maintains this design philosophy all the way onto the silicon of a high impedance amplifier,

The issue of stray capacitances is a significant one. A typical coaxial cable has a capacitance of around 30pF per foot. If coaxial leads were to have been used going from the electrometers to the sample, taking practical cable lengths, there would have been a stray capacitance in excess of 100pF per lead, which would have contributed over 100s to the time constant of a sample with an impedance of $10^{12}\Omega$. The wiring of the cryostat has an unknown capacitance.

2.4.2. A custom insert for the PPMS

Some of the effects that were seen in the initial measurements made on these composites were unexpected. It turned out that the measurements made using the wiring in the cryostat contained artifacts.

It was decided to construct an insert for the PPMS system that would provide guarding for all signal lines going to the sample under test, ending at most a few millimeters away from the test sample. All circuit boards in the system would also require all signal traces to be guarded. It is not possible to construct a four-wire setup where the surface of the sample itself is guarded. The surface of the samples in question seemed to be completely insulating (as discussed in section 3.3.1) and processing electrodes on to the sample required plasma-etching the sample, a process that would remove any organic contaminants. It therefore seemed unlikely that conduction across the surface of the sample was going to affect the measurements. The guard signals were available on the circuit board on which the sample was mounted, so it would be possible to do a conventional 2- wire guarded measurement using this custom-made insert.

Any heat leaks going into a cryostat had to be kept to a minimum. For this reason, all electrical conductors going in from the top of the cryostat were made of stainless steel 316 tubes. The top of the insert for the cryostat would have a flange with three hermetic triaxial connectors on it. Triaxial connectors are used on the inputs of the electrometers in use, and on the output of the current source. They are similar to BNC connectors, but differ in the fact that they have an inner shield that is used to guard the signal. The triaxial leads going down to the cold zone of the cryostat consisted of three tubes inside each other, the largest of which had a diameter of 0.23"; this being a limitation imposed by the dimensions of the cryostat.

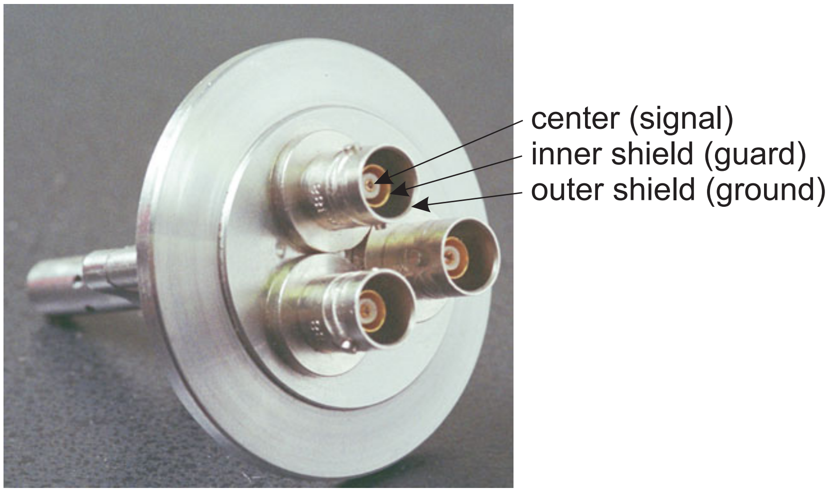

Figure 2.7 The flange for the insert that sits at the top of the cryostat.

The insert that was built is shown In Figure 2.8. There is a copper block at the bottom that extends the height of the cold zone of the PPMS. This copper block initially had spring fingers at its top and bottom: the ones at the top unfortunately came off due to the soldering failing with temperature cycling, leaving just the bottom ones. It was not easy to reattach them with the insert in a fully assembled state, but their loss did not seem to adversely affect its performance.

The temperature stability of the cold zone of the insert could easily be assessed by monitoring the resistance of the test samples. Going up from the cold zone to the flange at the top of the insert, the triaxial leads comprised three stainless steel tubes inside each other, all of identical material and temper, in thermal contact within the cold zone but not outside.

A test sample was attached to a circuit board (as shown in Figure 2.12b) which had all signal traces guarded. Wires that were not in physical contact with anything else went between this circuit board and the one internal to the insert, as can be seen in the close up of the cold zone in Figure 2.8. Whilst the possibility of having a single unit that contained all the wires was considered, to do this without risking the introduction of leakage current would not have been easy. Once the sample had been attached, a copper puck with spring fingers for contact with the cold zone of the PPMS was screwed onto the bottom of the insert.

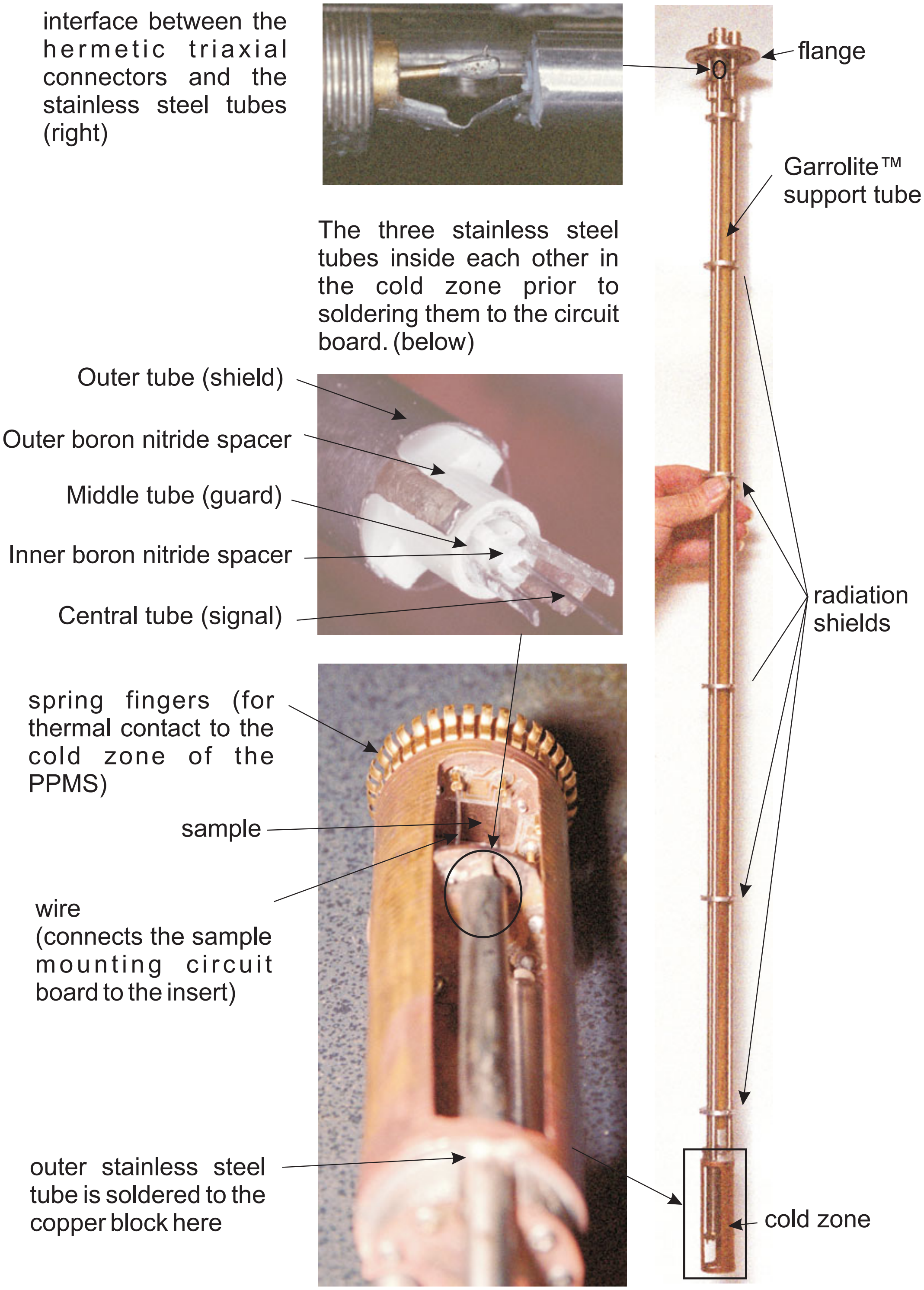

Figure 2.8 The custom insert for the cryostat that provides guarding of all signals.

Between the cold zone and the top of the cryostat, the spacers that separated the tubes were made of teflon, which conducts heat less well than the volume of helium gas that it replaced. To minimize differential thermoelectric effects, all three tubes were of the same material and temper. For the insert to work well, the tubes all had to be at the same temperature at the bottom. If the signal and guard were to be at different temperatures, the thermoelectric potentials of the tubes would be different, thus reducing the effectiveness of the guard. For this reason, within the uniform cold temperature zone, (the bottom three inches of the tubes) the three tubes were separated by boron nitride spacers – boron nitride being chosen for its high thermal conductivity and low electrical conductivity (see Figure 2.8). Throughout the entire length, the spacers were designed with gaps so that air could be pumped out and not trapped in the tubes, (see Figure 2.9).

Upon first evaluation of the insert on the table, it seemed that there might be a problem here, as the impedance between adjacent connectors was only a few megaohms. Upon placing the insert in a vacuum chamber, or PPMS system (which evacuates the chamber before filling it with helium), this impedance increased to greater than $10^{14}\Omega$ within 2 minutes: this increase was almost certainly due to condensed water within the tubes. When the insert was fabricated, the sequence with which it was put together necessitated removal of soldering flux using water at the end of fabrication. Although the problem of removing this water from the system turned out to be solvable by placing the unit in a vacuum chamber, if making the device again, I would not assemble it in exactly the same sequence. Minor design changes could make the thing less difficult to solder; easier to fabricate, and more robust in operation.

In Figure 2.8, the ends of the tubes are shown, with stainless steel tabs on the end that are later to be soldered to the circuit board in the insert. Tinning the tubes so that they could later be soldered to the circuit board did not work as planned. Acid flux had to be applied at the final step of soldering the tubes to the circuit board, with most of the insert assembled. If these tubes had been hard-soldered to some small copper parts tinned with electronic solder, they could have been thoroughly cleaned, before assembling all the spacers, leaving the final assembly step flux free, and the entire unit easier to repair. This is the approach I would take if making another of these devices.

Above the cold zone, the tubes were separated by the aforementioned teflon spacers – teflon having been chosen for its thermal and electrical insulation properties going from the cold zone to the top of the cryostat. The spacers were stacked up continuously along the entire length of the tubes. In this configuration, since the signal and guard tubes (see Figure 2.8) were at the same potential and temperature at both ends, thermoelectric effects should have affected them both equally, so they should both have been at the same potential at all points along their length. It was not possible to connect the tubes thermally to each other at points along their length without introducing a heat leak.

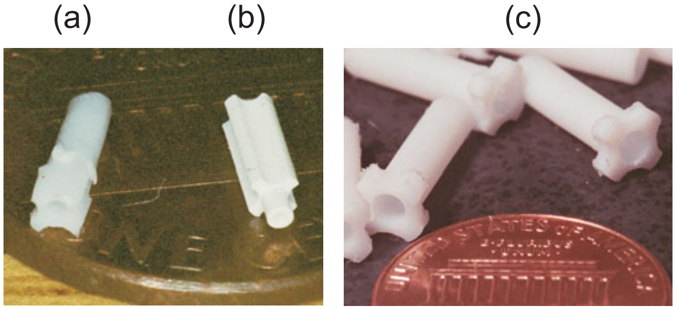

Figure 2.9 Spacers between the stainless steel tubes. (a) inner teflon spacers used from the top of the cold zone to the top of the cryostat (b) inner boron nitride spacers used in the cold zone, (c) outer teflon spacers used from the cold zone to the top of the cryostat. Pennies are present for scale.

Thermal contact with the sides of the cold zone was achieved by the use of the aforementioned spring-fingers, obtained from Quantum Design, and through the helium gas present. After consultation with Quantum Design, it was decided not to interface with the thermal and electrical connections at the bottom of the cryostat because it would have returned little benefit, and would have introduced many design problems, particularly those associated with thermal shrinkage as the cryostat is cooled down.

2.4.3. Performance of the custom insert for the PPMS

Construction of this custom insert accomplished perfectly the two goals that were intended - speed of measurement, and elimination of leakage. Speed of measurement was improved by a factor of 60, and the recorded data made much more sense. Using this insert the only limitation concerning the measurement of samples pertained to the electronics in use. It would have been interesting to investigate the possibility of measuring even higher impedance samples using three Keithley 6430's, but they were not available. Another limitation is that the insert cannot be used in air: it is suitable for use only in a dry atmosphere or a vacuum, so that samples cannot be tested with the insert on the laboratory bench.

When taking measurements using the insert, there were two major differences compared with connecting the same electronics using the wiring internal to the cryostat. Selected time-dependent recorded voltages V1 and V2 (defined in Figure 2.2) are shown in Figure 2.10. These measurements were taken using the same sample as the time-dependent measurements shown in Figure 2.6. When comparing Figure 2.4a with Figure 2.10a, both of which were recorded on the same sample at the same temperature, in the latter case, the meter readings were stable after less than 2 minutes, whilst in the former case, they were still not completely stable after 2 hours. The settling time using the insert did increase as the temperature was decreased, but even where the sample resistance exceeded 5TΩ (Figure 2.4c) it was still possible to obtain a measurement within 30 minutes.

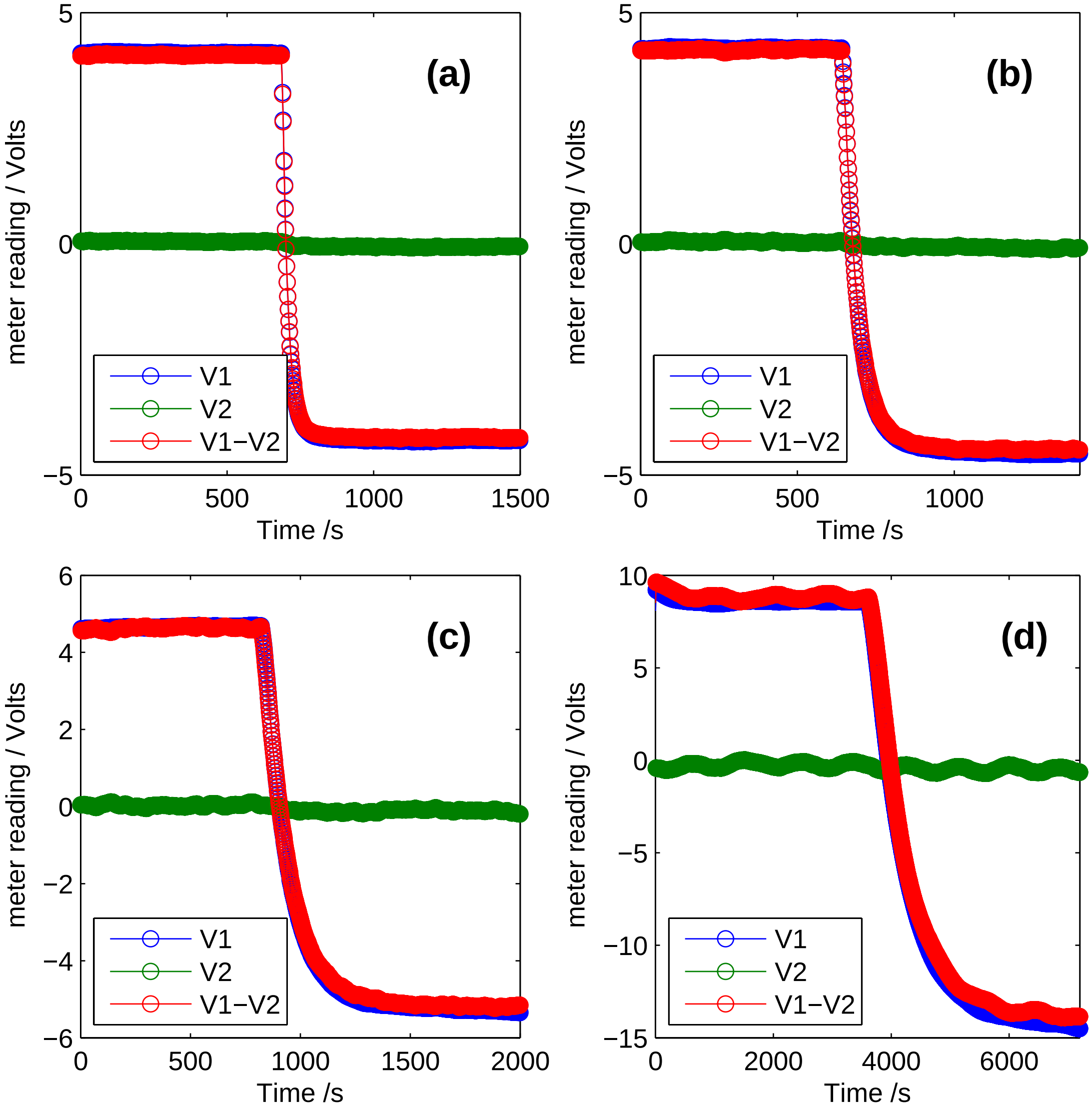

Figure 2.10 measured voltage V1 and V2 using the connections internal to the cryostat on a 4% composite sample kept at (a) 17K, programmed source current ±3.56pA, measured impedance 1.2TΩ (b) 16K, programmed source current ±1.74pA, measured impedance 2.5TΩ (c) 15K, programmed source current ±854fA measured impedance 5.7TΩ (d) 13K, programmed source current ±59.8fA measured impedance 19TΩ

The temperature dependence of the resistivity measured using the insert followed a VRH dependence all the way down to 15K (see Figure 2.11). The lowest temperature data point was a measured four wire impedance of 19TΩ. Since the electrometers in use are rated to have an input impedance >100TΩ, this last data point is not likely to be reliable. Bearing these measurements in mind, the experimental setup that has been built has an upper limit of around 5TΩ on the resistances that it can measure. For the remainder of this thesis, no data points that give an impedance greater than 5TΩ will be shown. With the equipment in use, it was not possible to carry out a simultaneous 4 wire measurement and a directly measured 2 wire measurement, since the current source does not measure its output voltage. The 2 wire measurement in Figure 2.11 was therefore measured on a separate occasion several months later than the 4 wire measurement on the same sample. It is also of note that when comparing the interface resistance as a function of temperature, this does not go up as fast when measured using the insert as when using the internal wiring of the cryostat. The most likely explanation is one of leakage current when using the wiring internal to the cryostat.

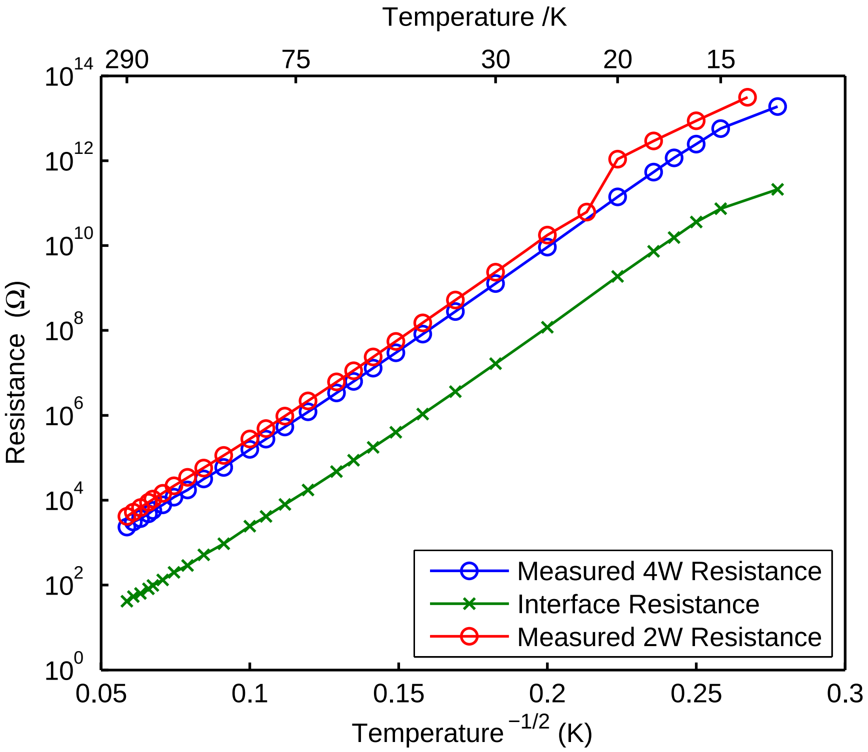

Figure 2.11 Resistance versus temperature for a 4% weight composite sample measured in the quantum design PPMS using the custom insert.

The commercially supplied sample puck that connects to the wiring internal to the PPMS is shown in Figure 2.12a. This puck is one example of a location where leakage current could have taken place. If the puck were to have any condensed water or grease on it from handling (either by my use, or that of previous users of the system), conduction could take place across the circuit board, thus lowering the measured resistance. In addition to current taking the short path between electrodes 2 and 3, it could also travel the long way around the circuit board, leading to a potential difference between electrodes 1 and 2, and 2 and 4. Such a current path would lead to a rise in the apparent measured interface resistance. There may be other points of current leakage in the PPMS wiring, of which not all of the design details are known.

The circuit board on which the sample was mounted prior to being placed in the custom insert is shown in Figure 2.12b. On this board, all signal pads were surrounded by guard traces held at the same potential as the signals. Since there was never any potential difference between a signal trace on the board and an adjacent trace, leakage current was greatly reduced

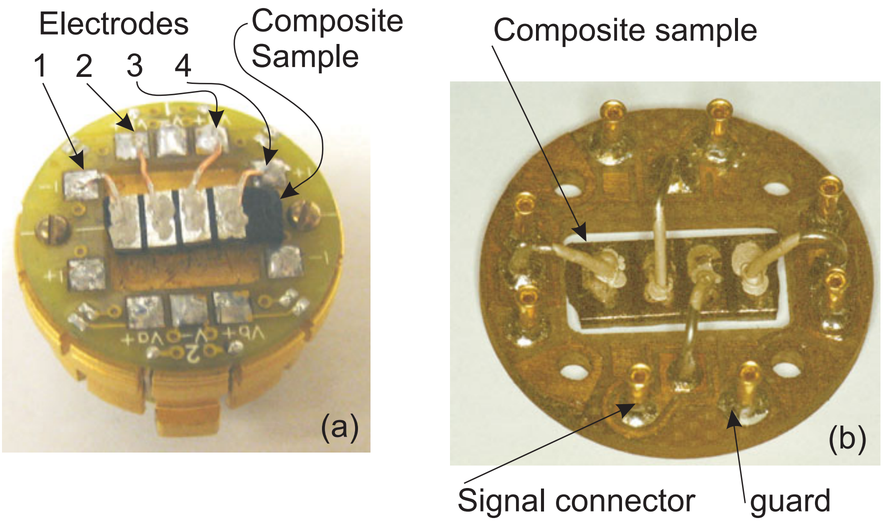

Figure 2.12 The pucks that the samples sit on (a) the supplied puck by quantum design that connects to the cabling internal to the cryostat, (b) the circuit board that the sample sits in for mounting using the custom insert.

2.4.4. Recording electrical data

The PPMS system is designed to be highly automated, capable of carrying out many experiments unattended. To get maximum use from the helium, it is necessary to run experiments 24hrs a day. The electrometers in use were not part of the PPMS system, and its software did not support them. Interfacing custom-designed software with the PPMS was relatively easy, as once its native software was closed down, the PPMS itself is just a GPIB device. It was therefore decided to write some custom software to support these electrometers.

The approach taken with the custom-made software was to read in a sequence file, where the available commands were to set the temperature, magnetic field, voltage limit that the current source would output, program the source current, and to start recording the voltages for a specified amount of time. During data taking, the current source was continually monitored to check that the programmed current was not too high for the given sample impedance. This was found to happen quite often because the sample resistance as a function of temperature was so variable, making it difficult to estimate suitable source currents with which to run the experiment. Thus, if the current source was attempting to source a current that was too high and therefore out of range, the software would automatically reduce the programmed source current by 20% and then restart recording the measured voltages. This is the reason why some data is taken in this thesis with seemingly arbitrary current values. In practice, it was only meaningful to take data in the regime where the resistance is linear, as discussed in 2.2.2.

The typical procedure for measuring composite samples was to limit the maximum applied voltage to 5 volts, and then let the software choose the current. Room-temperature data was taken with a limit of 1 volt for most of the composite samples.

3. Graphene-based nanocomposite materials.

The starting point for the graphene-based materials studied in this work was a suspension of nanosheets, prepared by a solution process[10] from exfoliated graphite oxide. Graphite oxide was prepared by the Hummers method from SP-1 graphite (Bay Carbon), and dried for a week over phosphorus pentoxide in a vacuum desiccator. Dried graphite oxide (50 mg) was suspended in anhydrous dimethylformamide (5 ml, Dow-Grubbs solvent system), treated with phenyl isocyanate (2 mmol, Sigma-Aldrich) for 24 h, and recovered by filtration through a sintered glass funnel (50 ml, medium porosity). Stable dispersions of the resulting phenyl isocyanate-treated graphite oxide materials were prepared by ultrasonic exfoliation (Fisher Scientific FS60, 150W, 1 h) in DMF (1mg ml^{-1}). Atomic force microscopy of the exfoliated graphite oxide when placed on mica and allowed to dry down is shown in Figure 3.1. The platelets are almost certainly individual sheets, since their measured thicknesses are all similar, around 1nm. The small particles visible are a yet-to-be identified salt. They can be removed by briefly rinsing the surface of the mica with de-ionized water. Attempts to purify the solution by dialysis have so far been unsuccessful, adding more contamination than the process removed. The lateral dimensions of the sheets were limited by the ultrasonic method of exfoliation. The solution could also be exfoliated by stirring it for a month. Solutions prepared this way had sheets that were laterally much larger as can be seen from Figure 3.2. In this case, the sheets were so large that they tended to wrinkle when deposited on a substrate, and the full extent of the sheet could not be covered by a 15µm scan. It can be seen from the line profile that in this case a single sheet is about 0.6nm thick or multiples thereof; thinner than in the case of sheets prepared by ultra-sonication. All materials studied in this work are however from solutions prepared by ultra-sonication.

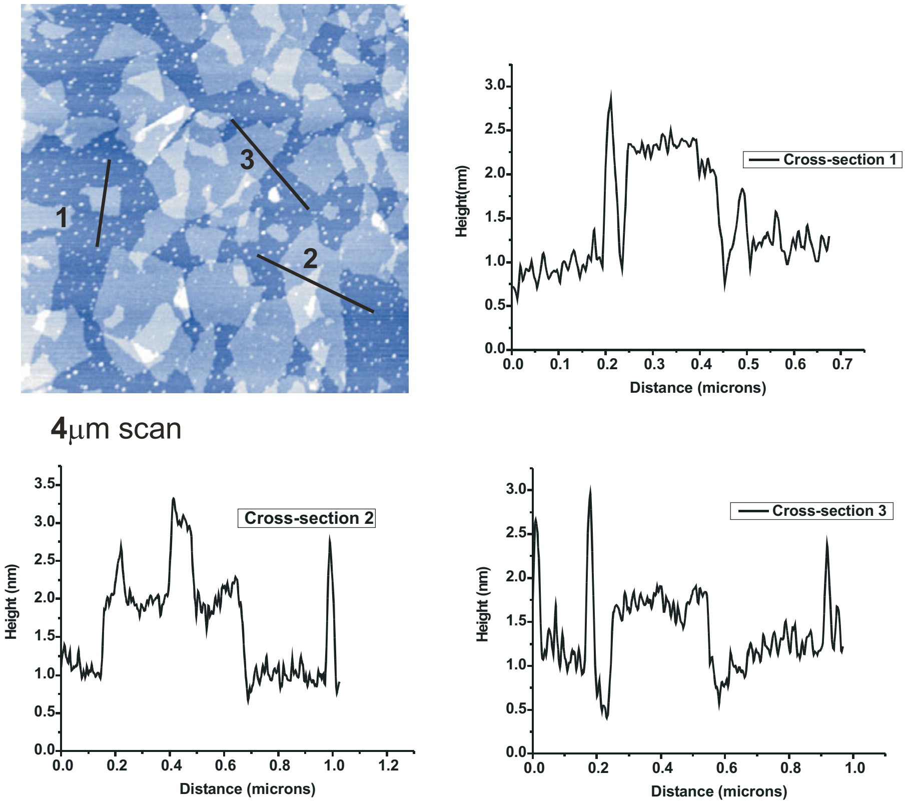

Figure 3.1 Atomic force microscopy of a dried down suspension of exfoliated graphite oxide that has been exfoliated by ultrasonication.

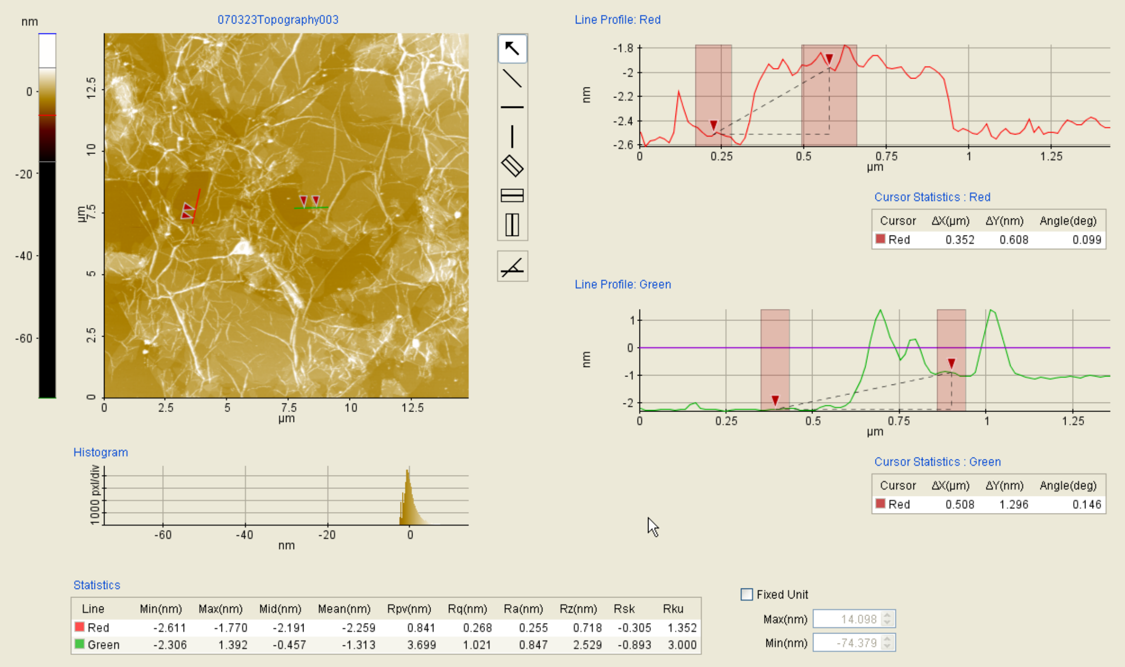

Cursor Statistics : Red

Cursor	ΔX(μm)	ΔY(nm)	Angle(deg)
🟥 Red	0.352	0.608	0.099

Cursor Statistics : Green

Cursor	ΔX(μm)	ΔY(nm)	Angle(deg)
🟥 Red	0.508	1.296	0.146

Statistics

Line	Min(nm)	Max(nm)	Mid(nm)	Mean(nm)	Rpv(nm)	Rq(nm)	Ra(nm)	Rz(nm)	Rsk	Rku
🟥 Red	-2.611	-1.770	-2.191	-2.259	0.841	0.268	0.255	0.718	-0.305	1.352
🟩 Green	-2.306	1.392	-0.457	-1.313	3.699	1.021	0.847	2.529	-0.893	3.000

☐ Fixed Unit

Max(nm) 14.098

Min(nm) -74.379

Figure 3.2 Atomic force microscopy of a dried down suspension of exfoliated graphite oxide that has been exfoliated by stirring.

3.1. Fabrication of a graphene-based nano-composite in a polystyrene matrix

To form the nanocomposite, polystyrene (Scientific Polymer Products, approximate M_w = 280 kD, polydispersity index = 3.0) was added to the dispersions of nano-platelets, and dissolved by stirring. Reduction of the dispersed material was carried out with dimethylhydrazine (0.1 ml in 10 ml of DMF, Sigma-Aldrich) at 80ºC for 24 h. Upon completion, the coagulation of the polymer composites was accomplished by adding the DMF solutions drop by drop into a large volume of vigorously stirred methanol (10:1 with respect to the volume of DMF used). It was this last step that placed practical limits on the amount of material that could be produced by this method. The coagulated composite powder was isolated via filtration; washed with methanol, and dried at 130°C under vacuum for 10 h to remove residual solvent, anti-solvent, and moisture. Drying the material under vacuum had a visible effect on the material. As shown in Figure 3.3, before drying, the composite was a grey, flakey powder that a simple multi-meter test showed was not electrically conductive. After drying, the composite became a black, stuck-together powder, much smaller in volume that was electrically conductive. A process flow diagram for the entire fabrication process is shown in Figure 3.4. It is of note, that thorough vacuum drying was required for the composite to be electrically conductive. If it was not vacuum dried for long enough, the composite was electrically insulating whatever further processing was applied to it.

It is of note that graphite oxide will exfoliate in water without the isocyanate treatment. It is however impossible to make composites by this approach because water is not a solvent of most polymers. This is the reason why it was necessary to treat the graphite oxide so that it would exfoliate into DMF, which is also a solvent of polystyrene.

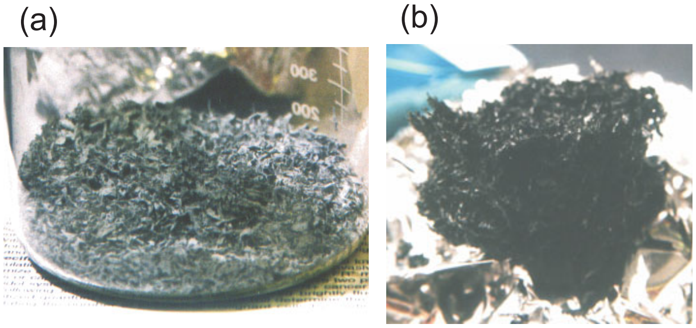

Figure 3.3 Nano- composite powder that has been fabricated by the solution based approach (a) before vacuum drying when it is a grey powder, (b) after drying when it is black, coagulated and electrically conductive.

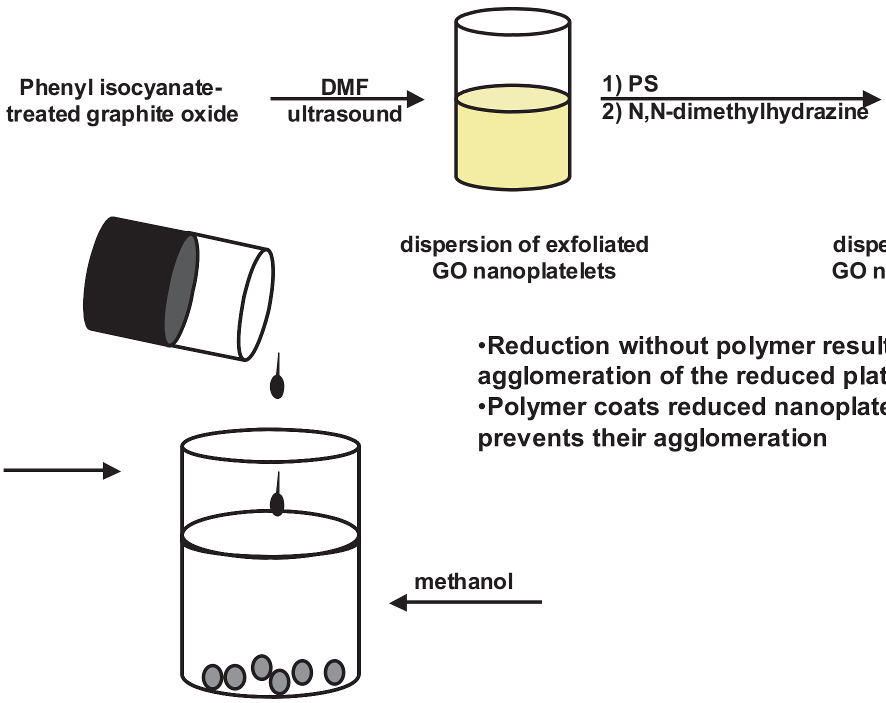

Figure 3.4 Process for the entire fabrication process of making the graphene-based nanocomposite.

The dried composite powder was formed into solid plastic samples by two methods: hot pressing and injection molding. To make hot pressed samples, the composite powder was first crushed with a mortar and pestle, and then placed between two brass plates in a hot press with 0.3mm thick spacers between the plates. Before placing the composite on the plates, mold release (Sprayon™ urethane and styrene silicone) was applied to the plates to facilitate the eventual release of the resulting material. Pressure was applied, and the press was ramped up to 220ºC and back down again, which took approximately 2 hours. The rate of flow of the polymer would have been extremely low. The resulting samples were then cut into 5-mm wide strips

Injection molding as a method of making composite samples was chosen as it is a common method for industrially made plastic parts. Samples were fabricated using a molder as discussed is section 2.1.2. Dried composite powder and fracture surfaces of samples were characterized by scanning electron microscopy (SEM; Leo 1525, Carl Zeiss SMT Inc. and Nova Nano SEM 600, FEI Co.). In all samples, the sheets were seen to be well dispersed.

3.2. Conduction Mechanisms that are commonly applied to carbon polymer composites.

A polymer composite having single graphene sheets as the filler material is new, although there is extensive literature concerning carbon-polymer composites. In particular, some carbon black composites, which have been studied extensively, consist of hollow shells that are only a few layers of graphene thick. It is therefore reasonable to expect some similarities in the properties of the nano-plate system being studied here with some of the carbon black systems that have been extensively studied in the past.

In a disordered system, such as a polymer composite, a variety of phenomena including localization effects, hopping transport, percolation, and tunneling can play a role[11-13]. The mechanism of conduction may also depend on the concentration of filler in the composite[14]. Since polymers expand upon heating, if the network of conductive filler is not continuous and the electrons are simply tunneling from one conductive object to another, the resistance should increase with temperature and also be a function of the applied voltage[15-18.] There are however some methods of conduction in composite materials where the conductivity does increase rather than decrease with increasing temperature, namely thermally activated tunneling, and hopping. These mechanisms of conduction can be probed by measuring the temperature dependence of the material's resistivity.

3.2.1. Thermally activated tunneling

The thermally activated tunneling model is described elsewhere[19,20]. The basics of this model are as follows. The composite is assumed to consist of conductive particles that are dispersed in an insulating matrix that separates them. Electrical conduction through the bulk material takes place as electrons tunnel between these conductive particles. The conductive particles are assumed to be large enough so that the transfer of an electron between any two of the particles does not cause significant charging of either particle. In addition, the junction is modeled as two parallel plates with separation *w* and area *A*. These two areas are now taken to be separated by a symmetrical potential barrier, $V(x)$, that can be written in the form $V(x) = V_0 - \beta^2 x^2 - \beta^4 x^4 \ldots$ where $x = 0$ is defined as being the center of the junction. Ignoring terms of higher order than x^2, this gives a barrier potential of the form:

$$V(x) = V_0 - \frac{4V_0}{w^2} x^2 \qquad 3.1$$

In the WKB approximation, ignoring the backflow current, when an electric field ε is applied to the junction, the tunneling current density *j* between two parallel plates with such a barrier potential has the form:

$$j(\varepsilon) = j_0 \exp\left[-\frac{\pi \chi w}{2} \left(\frac{|\varepsilon|}{\varepsilon_0} - 1 \right)^2 \right] \qquad 3.2$$

Where the tunneling constant $\chi \equiv \left(2mV_0 / \hbar^2\right)^{1/2}$, *m* in the electron mass, $\varepsilon_0 \equiv 4V_0 / ew$, and j_0 is the pre-exponential factor that contains all the weak temperature and field variations of *j*. As the bulk material is at a non zero temperature, the junction is in a thermal bath, resulting in voltage fluctuations across the gap. These will have the form:

$$V = \left(\frac{kT}{C}\right)^{\frac{1}{2}} = \left(kT\frac{4\pi w}{A}\right)^{\frac{1}{2}} \qquad 3.3$$

where C is the capacitance of the junction, and *k* is the Boltzman constant.

A field induced by a thermal fluctuation can be either in the forwards or backwards direction. The net forwards tunneling current is:

$$\Delta j = j(\varepsilon_A + \varepsilon_T) - j(\varepsilon_A - \varepsilon_T) \qquad 3.4$$

Where ε_A is the applied electric field across the junction, and ε_T is the thermally fluctuating electric field across the junction. A partial conductivity $\sum(\varepsilon_T)$ can be defined by:

$$\Sigma(\varepsilon_T) = \lim_{\varepsilon_A \to 0}\left(\frac{\Delta j}{\varepsilon_A}\right) = 2\frac{dj(\varepsilon_T)}{d\varepsilon_T} \qquad 3.5$$

From $\sum(\varepsilon_T)$, the conductivity of the junction σ can be obtained by thermal averaging:

$$\sigma = \int_0^\infty P(\varepsilon_T)\Sigma(\varepsilon_T)d\varepsilon_T \qquad 3.6$$

Where $P(\varepsilon_T)$ is the probability of observing the field ε_T due to thermal fluctuations. Substitution of 3.2 and 3.5 into 3.6 and saddle point integration leads to the conductivity for a single junction being given by

$$\sigma = \sigma_0 \exp - \left\{\frac{T_1}{T + T_0}\right\} \qquad 3.7$$

It can however be shown[21] that with reasonable distributions for T_0 and T_1 that the conductivity of the network is similar to that of the single junction.

This model has been applied to many carbon-polymer composites, successfully at low temperatures[22-24]. It should be kept in mind that the underlying assumption of this model is that the electrons are transferring between the edges of islands that are metallic in nature. The distance over which the transfer between the islands takes place is smaller than the islands. Since the particles in the graphene based nano-composite are too small for it to be likely that the metallic continuum will hold true, it is not surprising that this model is a very bad fit for the experimental data regarding the nano-composite material that will be discussed later.

3.2.2. Mott Variable Range Hopping (VRH)

The Mott VRH model was first proposed by Mott[25] in 1968, and subsequently developed.[26-28] Conduction through the bulk material is described as taking place via thermally assisted hopping of electrons between states that are localized near randomly distributed sites. It was originally used for describing conductivity of amorphous germanium at low temperature, which has the temperature-dependent conductivity, as shown in equation 3.8. where ρ is the resistivity of the material, a is the localization radius of states near the Fermi level, $g(\mu)$ is the density of states at the Fermi level, and β is a numerical coefficient which Mott did not originally determine. For this model to be valid, the dopants in the semiconductor must be of sufficiently low concentration that their electronic states are spatially isolated, and a band structure is not formed. The temperature dependent resistivity in this case is given by:

$$\rho(T) = \rho_0 \exp\left[(T_0/T)^{1/n}\right] \qquad \text{where} \qquad 3.8$$

$$T_0 = \frac{\beta}{k_B g(\mu) a^3} \qquad 3.9$$

And n = 4 for three dimensional conduction

The derivation that follows in the rest of this section and in section 3.2.3 is an outline of what is presented by Shklovskii and Efros[40], which should be referred to for more detail. What is presented here is intended to illustrate the physical origin of the hopping model.

To calculate the resistivity of a material with electron wave functions isolated on individual donors, Miller and Abrahams[29] suggested the following. Calculate the probability that an electron transition will occur between two donors i and j with the absorption or emission of a phonon, then calculate the number of transitions $i \rightarrow j$ per unit time. In a weak electric field, the forward and reverse transitions will not balance, giving rise to a current that is proportional to the field. Evaluating this gives a resistance R_{ij} for a given transition, reducing the bulk conduction to that of solving a random network of resistors. It can be shown that each resistance for an arbitrary ε_i^0 and ε_j^0 with respect to the Fermi level can be given by:

$$R_{ij} = R_{ij}^0 \exp(\xi_{ij}) \qquad \text{where} \qquad 3.10$$

$$\xi_{ij} = \frac{2r_{ij}}{a} + \frac{\varepsilon_{ij}}{k_B T} \qquad \text{and} \qquad 3.11$$

$$R_{ij}^0 = \frac{k_B T}{e^2 \gamma_{ij}^0} \qquad \text{and} \qquad 3.12$$

$$\varepsilon_{ij} = 1/2\left(\left|\varepsilon_i - \varepsilon_j\right| + \left|\varepsilon_i - \varepsilon_f\right| + \left|\varepsilon_j - \varepsilon_f\right|\right) \qquad 3.13$$

where a is the localization radius of the states, γ is the transition probability between two states, and ε_f is the Fermi energy.

Consider a system with localized states near the Fermi level. Since 3.10 contains a term that is exponential in ε_{ij} at low temperatures, only resistances having small ε_{ij} will contribute significantly to conduction. Also, at sufficiently low temperature, the density of states can be regarded as constant $g(\varepsilon)=g(\varepsilon_f)$ so long as $g(\varepsilon_f)\neq 0$.

Consider the conductivity resulting from energy levels within a small band that is symmetric about the Fermi level such that:

$$\left|\varepsilon_i-\varepsilon_f\right|\leq \varepsilon_0 \qquad 3.14$$

The concentration of states in the band given by 3.14 is given by:

$$N(\varepsilon_0)=2g(\mu)\varepsilon_0 \qquad 3.15$$

Using 3.10 estimate the resistance corresponding to two typical states in the band given by 3.14. On replacing r_{ij} with the typical separation between sites $[N(\varepsilon_0)]^{-1/3}$ and replacing ε_{ij} with ε_0 the expression for the resulting resistivity from the energy band ε_0 is given by:

$$\rho=\rho_0\exp\left[\frac{1}{N^{1/3}(\varepsilon_0)a}+\frac{\varepsilon_0}{k_BT}\right]=\rho_0\exp\left[\frac{1}{[g(\mu)\varepsilon_0]^{1/3}a}+\frac{\varepsilon_0}{k_BT}\right] \qquad 3.16$$

Because of competition between overlap and activation as a function of ε_0, equation 3.16 has a sharp minimum at:

$$\varepsilon_0=\varepsilon_0(T)\equiv\frac{(k_BT)^{3/4}}{[g(\mu)a^3]^{1/4}} \qquad 3.17$$

Upon substituting 3.17 into 3.16, Mott's law, 3.8 and 3.9 can be obtained. A more rigorous derivation[30] using percolation theory can be used, and gives a value of $\beta=13.8\pm0.8$ for three dimensional conduction[31]. It is also of note, that in this conduction regime, as the temperature of the system decreases, the average hopping length increases, the average hopping length scaling with $a(T_0/T)^{1/4}$.

The exponent in 3.8 can be modified. If conduction is limited to two dimensions, a similar derivation will yield n=3 in equation 3.8, since the separation between sites will be $[N(\varepsilon_0)]^{-1/2}$ instead of $[N(\varepsilon_0)]^{-1/3}$. However, since in the systems discussed in this work, we are considering plates of material that are order of magnitude a millimeter thick, this is not likely to be relevant to this work.

3.2.3. Efros-Shklovskii Variable Range Hopping (ES-VRH)

Consider the case where the density of states $g(\varepsilon)\to 0$ at the Fermi energy. Pollak[32] and Hamilton[33] considered the case where the density of states decreases according to the law:

$$g(\varepsilon)=g'\left(\frac{|\varepsilon-\varepsilon_f|}{\varepsilon'}\right)^m \qquad \text{where m>0} \qquad 3.18$$

Equation 3.15 now becomes:

$$E(\varepsilon_0)=g'\int_{\varepsilon_f-\varepsilon_0}^{\varepsilon_f+\varepsilon_0}\left(\frac{|\varepsilon-\varepsilon_f|}{\varepsilon'}\right)^m d\varepsilon=\frac{2}{m+1}\frac{g'\varepsilon_0^{m+1}}{(\varepsilon')^m} \qquad 3.19$$

Repeating the derivation in section 3.2.2 will again yield an expression of the form 3.8, but with:

$$n=\frac{m+1}{m+4} \qquad 3.20$$

According to Efros and Shklovskii[28], if there is a zero density of states at the Fermi energy caused by interaction between the donor sites that manifests itself, the density of states must be parabolic, yielding a value of m =2 in equation 3.20. Thus the ES-VHR model is given by:

$$\sigma(T) = \sigma_0 \exp\left(-\left(\frac{T_0}{T}\right)^{\frac{1}{2}}\right) \qquad 3.21$$

3.3. Electrical properties of a graphene-based nano-composite in a polystyrene matrix

Composite powder was prepared by our solution-based chemical approach as described in section 3.1. The dried composite powder was formed into solid plastic samples by two methods: hot pressing and injection molding. To make hot pressed samples the composite powder was first crushed with a mortar and pestle, and then placed between two brass plates in a polymer hot press with 0.3mm thick spacers between the plates. Before placing the composite on the plates, mold release (Sprayon™ urethane and styrene silicone) was applied to the plates to facilitate the eventual release of the resulting material. Pressure was applied, and the press was ramped up to 220ºC and back down again, which took approximately 2 hours. The rate of flow of the polymer would have been extremely low. The resulting samples were then cut into 5-mm wide strips.

Injection molding as a method of making composite samples was chosen, as it is a common method for industrially made plastic parts. If the material is to have applications dependent upon such processing, how this method of manufacture affects the material's properties will be important. Molding should also be a more controllable and repeatable process than hot pressing. As available quantities of composite material were limited, we designed and fabricated a custom mold that needed only 3 grams of composite powder for one fabrication cycle as described in section 2.1.2. The mold was heated to 140ºC and the molten material pushed rapidly through a 1-mm hole into a 5-mm wide and 1-mm thick cavity. The duration of this flow was less than 1 second. The inside of the cavity was also coated with the same polystyrene mold release to facilitate release of the composite samples from the mold.

3.3.1. Dispersion of the platelets within the composite

Dried composite powder and fracture surfaces of samples were characterized by scanning electron microscopy (SEM; Leo 1525, Carl Zeiss SMT Inc. and Nova Nano SEM 600, FEI Co.). Typical SEM images of hot pressed samples are shown in Figure 3.5, and that of molded samples are shown in Figure 3.6 In all samples, the sheets were seen to be well dispersed, though they do exhibit more alignment in the latter case.

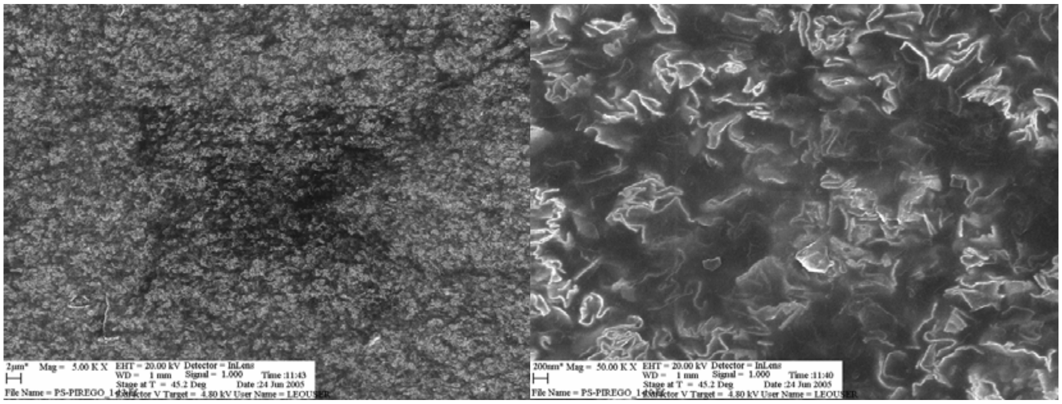

Figure 3.5 SEM of a fracture surface of hot pressed 1% weight chemically modified graphene sheets in in polystyrene.

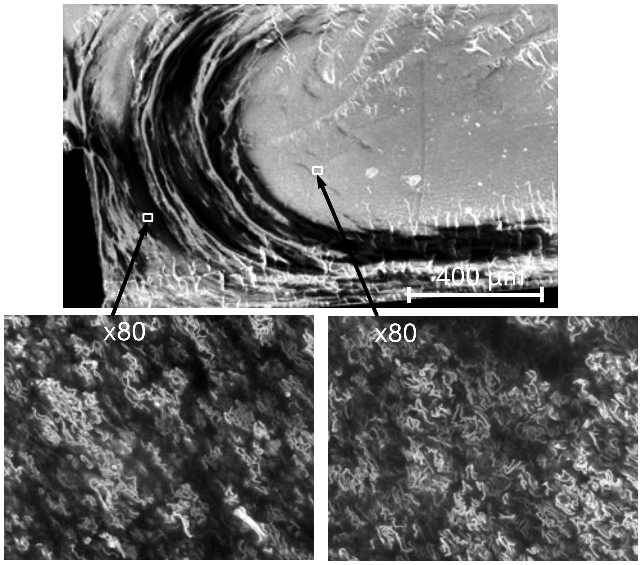

Figure 3.6 SEM images of fracture surface of composite containing 0.5% weight of chemically modified graphene sheets in polystyrene that was prepared by injection molding and then annealed; higher magnification images obtained in the indicated regions.

The surface of the composite, whether prepared by hot pressing of injection molding had a layer several microns thick that had a very low concentration of graphene based sheets. To obtain good electrical contact, hot pressed or molded samples were oxygen plasma-etched for 90 seconds using a Kurt Lesker Plasma Preen II-862 operating at 350W. Without this step, the interface between the composite and the electrodes were found to have a very high resistance. After etching, 100nm of silver was evaporated through a mask using an Edwards Auto-306 thermal evaporator to form a row of 4 electrodes that were 2-mm wide with a space of 0.5 mm between them,

3.3.2. Qualitative Electrical properties

Temperature-dependent electrical resistance was then measured in a Physical Properties Measurement System (PPMS; Quantum Design, San Diego, CA). The resistance of the samples increased as temperature decreased and exceeded $10^{12}\Omega$ at low temperature. To be able to measure these high impedances, a Keithley 6415 Current source and 2 Keithley 6115 electrometers with an input impedance $>10^{14}\Omega$ were used to measure the four-terminal voltage with the configuration as discussed in section 2.2.1. and the sample was mounted in a custom insert for the cryostat as discussed in section 2.4.2

The point of this study was to measure the bulk properties of the material. As the composite is a two-phase system, a measurement across a small part of the sample could potentially be unrepresentative of the whole sample. To ensure that the bulk properties of the composite were being measured, all sample dimensions had to be very much greater than the largest dimension of the graphene-based sheets(~1μm). When this constraint was combined with the confined geometry of the PPMS cryostat and the high resistivity of the material under test, it was not possible to construct the samples in such a way as to keep the spacing between the electrodes very much greater than the thickness of the sample. This geometry resulted in a non-uniform current distribution within the sample. A finite element model described in section 2.2.2 was used to account for this.

The dried composite powder that both types of samples were formed from was found to be electrically conductive by touching a grain with multi-meter probes. Samples that had been hot-pressed were found to be electrically conductive with no further processing. Those that were molded had a resistivity > $10^{10}\ \Omega\ m^{-1}$, the upper limit of our experimental setup. Molded samples were found to be non-conductive throughout all parts of the sample – removing material from the surface had no effect. However, the molded samples could reversibly be made conductive by annealing. Breaking up and remolding the material made conductive by annealing, rendered it non-conductive again. This process could be repeated several times – though with each cycle, the material then became more brittle, presumably because of thermal degradation of the polystyrene. By comparison, annealing the hot-pressed samples had no effect on their conductivity.

In molded samples, the rate at which the conductivity increased as a result of this annealing process was found to depend on both temperature and the concentration of the sheets. After annealing for sufficient time such that further annealing had little effect, the final room-temperature resistance of the material was found to be independent of the temperature at which the composite was annealed to within the limits of our experiments. Unfortunately, significant sample deformation took place at the elevated temperatures, making an accurate comparison of the final resistivities of different samples impossible.

3.3.3. Time-dependent electrical properties of injection molded nano-composites at elevated temperature

The time-dependent, electrical properties of composite samples were measured by attaching a sample to a glass slide. The sample was then placed in a tube furnace with a thermocouple close by to monitor the temperature. Resistance data was taken using a standard multi-meter to measure the sense voltage. The wires going to the sample in the tube furnace were shielded. Even so, the limit of reliable resistance measurements with this arrangement was little more than a few 10's of MΩ, limited by electromagnetic interference from the furnace. The high impedance electrometers were not available for this project at the time that these experiments were started. This was not considered a limitation because the resistance of the samples at the elevated temperatures was not great, except for right at the beginning of an annealing experiment, but it was not a limitation here either since EM interference from the tube furnace was a greater problem than the impedance of the multi-meters.

A plot showing both temperature and resistance for a 5% weight injection-molded nano-filler composite sample is shown in Figure 3.7 As the composite was annealed, the resistance dropped. When the composite was maintained at an elevated temperature for a long enough time period, the resistance started to rise slightly, as can be seen from Figure 3.7. This small rise was attributed to thermal degradation of the polymer, and was therefore not considered in detail. By comparison, annealing hot- pressed samples had a minimal effect on the resistance of the samples. What changes were seen were small increases in resistance, again presumably because of thermal degradation of the polymer.

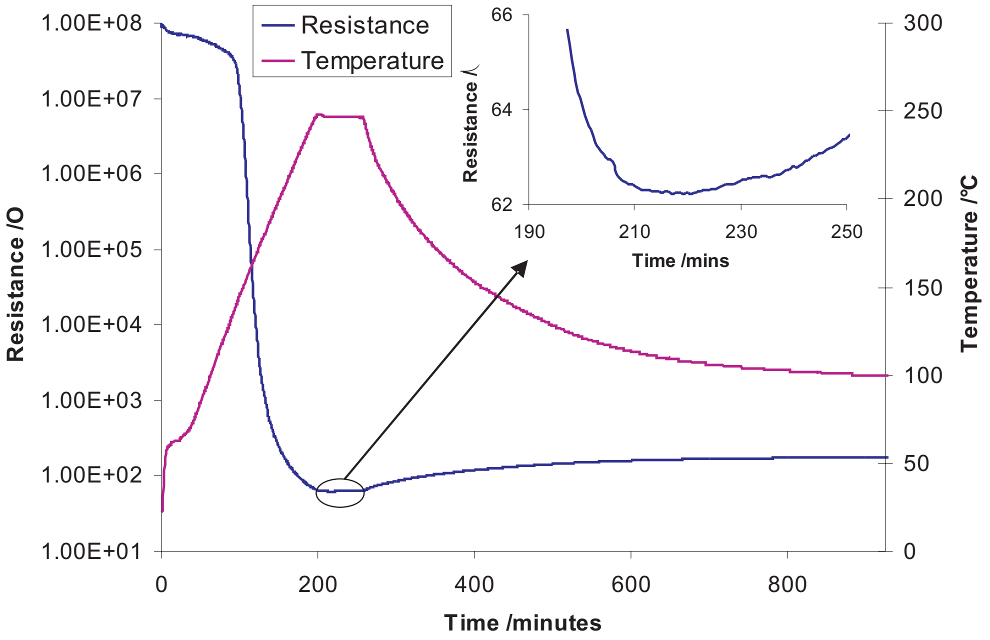

Figure 3.7 Resistance of molded 5%wt CREGO in polystyrene sample as it is annealed. During the time that the temperature is kept constant at 247°C, the resistance increases slightly

The temperature threshold at which annealing occurred decreased as the concentration of sheets increased. The rate at which this annealing took place also increased with increasing sheet concentration, as can be seen from Figure 3.8.

A reduction in the conductivity of a carbon polymer composite by high shear flow, and subsequent restoration of conductivity by annealing is not unique[34,35], however, in the case of nanofillers, the mechanism is not yet clear. In the case of the hot-pressed samples, SEM imaging shows that the sheets are unaligned, see Figure 3.5. In the case of injection-molded samples, one might expect the shear flow during the molding process to cause some alignment of the particles. For the non-conductive samples, high resolution SEM imaging proved difficult, with very low contrast between the sheets and the polymer. SEM images of injection-molded samples that had been annealed (and thus rendered conductive) are shown in Figure 3.6. It can be seen that after this annealing process, the sheets have some alignment, becoming less aligned towards the center of the sample than at the edges. Regardless of whether the sheets were aligned or not, the composite could be conductive. For this reason, and other reasons that will be discussed later, it is unlikely that the change in conductivity arose from a change of sheet geometry (or alignment) during the annealing process.

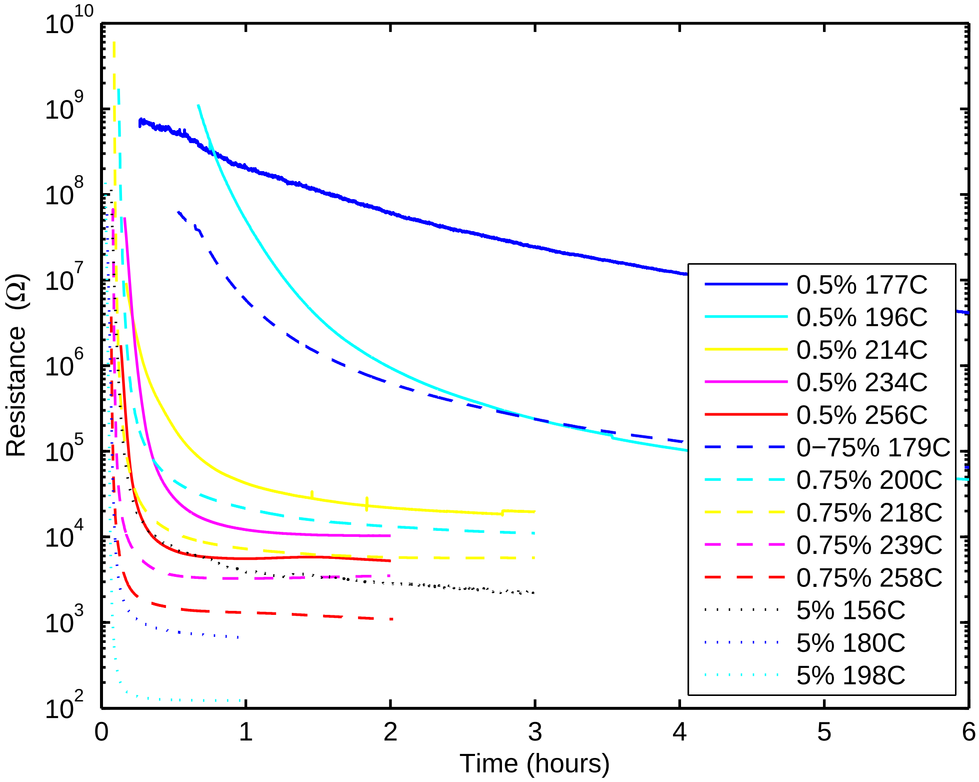

Figure 3.8 Resistance vs time as composite samples are annealed

3.3.4. Temperature dependent properties of the composite

The temperature dependent conductivity σ of the composites was measured over the temperature range of 10 – 300K. Below 10K, the sample resistance became too great to measure. When the data is plotted in the form of log σ vs T^{-1} the slopes do not form straight lines but decrease with decreasing temperature, suggesting that the conduction occurs by a variable range hopping process.[23,28]

Tunneling, previously mentioned as a possible model does not fit the experimental data. Variable range hopping has previously been applied to some high surface area carbon black systems[24,36-40.] Mott's variable range hopping has been found to be applicable to carbon nanotube mats[41-44.] The Efros-Shklovskii VRH model has been claimed to be applicable to nano-graphite networks[45], iron carbide polymer composites[46] amorphous carbon films[23] and SWNT / PMMA composites over a limited temperature range[47]. If a hopping model applies, then the conductivity is expected to be of the form:

$$\sigma = \sigma_0 \exp\left[-\left(T_0 / T\right)^n\right] \tag{3.22}$$

with n<1. Since all measurements taken are likely of the same accuracy, with the magnitude of the errors proportional to the magnitude of the measurement, least squares fitting using equation 3.22 would put enormous weight on the highest resistance measurements, and almost no weight on the measurements taken at the highest temperatures, where the magnitudes of the resistances are smallest. The values of σ_0, T_0 and n that best fit each sample were obtained by least squares fitting using the form:

$$\ln(\sigma) = \ln(\sigma_0) - \left(T_0 / T\right)^n \tag{3.23}$$

The fitted values for all samples tested are shown in Table 3.1. Since the values of n are grouped around 0.5, we also show the values for T_0 and σ_0, which are obtained by setting n=0.5, as this would be the form expected if we are in the ES-VHR regime. These values are designated as σ_0' and T_0'. We note that our values of T_0 and T_0' which have mean values of $T_0 = (1.15 \pm 0.46) \times 10^4\,\mathrm{K}$ and $T_0' = (1.42 \pm 0.19) \times 10^4\,\mathrm{K}$ have similar ranges as those identified by Dawson and Adkins, who carried out similar temperature dependent measurements and analysis on amorphous carbon films that were prepared by ion-beam sputtering[23]. Averaging the parameters of their amorphous carbon samples gives $T_0 = (2.3 \pm 1.1) \times 10^4\,\mathrm{K}$ and $T_0' = (1.29 \pm 0.30) \times 10^4\,\mathrm{K}$. Plots of log resistivity versus $T^{-1/2}$ are shown in Figure 3.9. Best fit straight lines are also shown. In the cases of both our composite, and the amorphous carbon films, the electron localization sites are likely to be sp^2 bonded carbon sites. It is possible that the similarity in hopping parameters is due to this.

The plots for the composite samples are essentially straight lines, indicating that ES-VHR hopping is a possible conduction mechanism for our composite samples at all concentrations, over a temperature range all the way up to 300K. T_0 is much greater than the temperature ranges looked at here, which is required for validity of any hopping model. Since we do not know neither the nature of the sites in the composite material that are contributing to the conduction, nor their density of states, we do not know if the parabolic density of states that is required for the ES-VHR mechanism is a result of a Coulomb interaction, or an intrinsic property of the sheets. It is of note that graphite is a zero-band, gap semiconductor, and since the sheets in the composite are of a graphitic-like structure, the possibility can not be ruled out that a vanishing density of states at the Fermi level might be due to an intrinsic property of the material.

Sample	n	σ_0	T_0	σ_0'	T_0'
Molded 1 wt% annealed 1hr	0.466 ± 0.026	$(1.524\pm0.038)\times10^{-2}$	$(1.802\pm0.025)\times10^{4}$	0.13+ 0.67 - 0.11	$(3.1\pm1.3)\times10^{4}$
Molded 1 wt% annealed 2hr	0.482 ± 0.013	2.41 ± 0.34	$(1.762\pm0.014)\times10^{4}$	7.7 + 10 – 4.4	$(2.33\pm0.47)\times10^{4}$
Molded 1 wt% annealed 4hr	0.493 ± 0.019	290 ± 60	$(1.783\pm0.019)\times10^{4}$	461 + 1200 – 330	$(1.98\pm0.58)\times10^{4}$
Molded 1 wt% annealed 8hr	0.5205 ± 0.0048	902 ± 110	$(1.768\pm0.011)\times10^{4}$	249 + 85 – 63	$(1.32\pm0.86)\times10^{4}$
0.5 wt % pressed	0.5695 ± 0.0067	58 ± 23	$(1.371\pm0.029)\times10^{4}$	1.67 + 0.6 - 0.44	$(5.76\pm0.42)\times10^{3}$
0.75 wt % pressed	0.566 ± 0.024	$(1.15\pm0.67)\times10^{3}$	$(1.357\pm0.036)\times10^{4}$	29 + 66 – 20	$(5.7\pm1.5)\times10^{3}$
0.8 wt% pressed	0.540 ± 0.022	$(1.18\pm0.46)\times10^{3}$	$(1.262\pm0.025)\times10^{4}$	124 + 280 – 86	$(7.3\pm2.0)\times10^{3}$
1 wt% pressed	0.513 ± 0.024	71 ± 17	$(1.885\pm0.024)\times10^{4}$	33 + 110 – 25	$(1.57\pm0.53)\times10^{4}$
1.5wt % pressed	0.562 ± 0.004	$(6.4\pm2.3)\times10^{4}$	$(1.178\pm0.023)\times10^{4}$	2609 + 540 – 450	5380± 242
2 wt% pressed	0.5643 ± 0.0031	$(1.27\pm0.49)\times10^{5}$	$(1.083\pm0.023)\times10^{4}$	5101+ 760 – 660	4834 ± 162
3 wt% pressed	0.5203 ± 0.0049	$(5.927\pm0.76)\times10^{3}$	$(1.255\pm0.094)\times10^{4}$	1872 + 509 – 450	9464 ± 618
4 wt% pressed	0.5503 ± 0.0084	$(5.9\pm2.2)\times10^{5}$	$(1.193\pm0.020)\times10^{4}$	$(3.0 +1.8 - 1.1)\times10^{4}$	6040 ± 616
5 wt% pressed	0.574 ± 0.011	$(8.0\pm4.1)\times10^{5}$	$(7.198\pm0.018)\times10^{3}$	$(2.3 +1.4 - 0.9)\times10^{4}$	2871 ± 334

Table 3.1 Variable range hopping parameters for the composites.

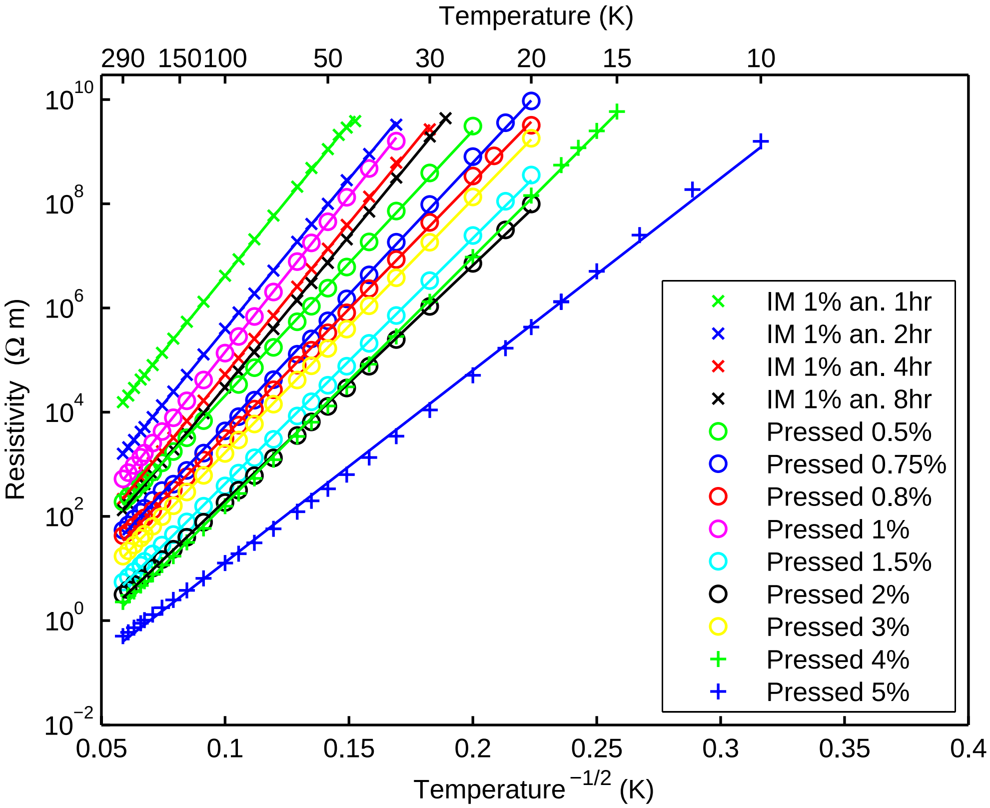

Figure 3.9 Resistivity versus $T^{-1/2}$ for both injection molded and hot pressed samples. Pressed = Hot Pressed, IM = Injection Molded, an. = time that the sample was annealed at 180°C. Best fit straight lines are also shown.

3.3.5. Annealing of insulating samples

Samples that were prepared by injection molding were initially non-conductive, but became conductive if they were annealed, as already mentioned. The time-dependent resistance of molded samples as they were annealed is shown in Figure 3.8. It can be seen that the rate of annealing is dependent on both the concentration of graphene based sheets and the temperature of annealing. The final resistances of samples having the same concentration of graphene based sheets but annealed at different temperatures differ because they are at different temperatures. All samples of the same concentration have the same resistance once they are cooled back to room temperature, irrespective of the temperature of annealing. If we use a hopping model, the resistance between any pair of sites depends exponentially on the distance between them. For three-dimensional conduction, the conductivity of the composite should therefore follow a dependence of the form[28]:

$$\sigma = \sigma_0 \exp\left(cN^{1/3}\right) \tag{3.24}$$

where c is a constant and N is the number of sites. Since the molecular weight of a sheet is unknown, and there is no way of estimating how the number of sites involved in the hopping conductivity is related to the number of sheets in the composite, I will take c to be a constant. Considering the concentration dependence across different samples, plotting $\ln(o)$ versus $N^{1/3}$ should yield a straight line. Such a plot for samples listed in Table 3.1 is shown in Figure 3.10. Unfortunately, Figure 3.10 resembles a scatter plot precluding a meaningful analysis of the concentration dependence looking across different samples. This scatter is most likely due to irreproducibility of the hot-pressing process. It is possible that better data could be obtained by using larger samples, or by averaging multiple samples of each concentration.

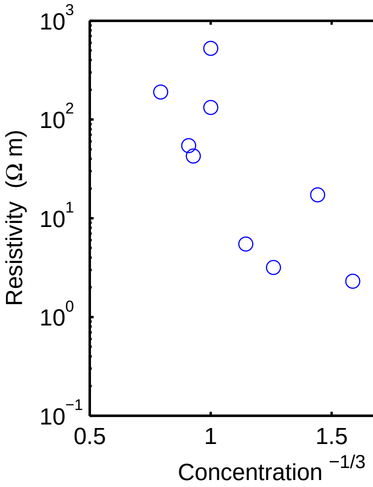

Figure 3.10 Room temperature resistivity versus weight percent filler concentration for the composite materials.

The time dependence of N for a single sample while it is annealed can be analyzed further. During the annealing process the samples could deform. By looking at the samples before and after annealing under a low magnification optical microscope, it was determined that although the electrodes were deformed, the spacing of the electrodes on the sample would change by at most a factor of 2 during the annealing process. It was therefore estimated that the change in geometry from mechanical deformation would account for at most a factor of 2 in the resistance. Since the change in resistance as a function of annealing exceeds 6 orders of magnitude, we regarded the change in resistance due to mechanical deformation, as negligible.

Assume that a freshly molded sample has N_0 sites that can potentially participate in a hopping conduction process, but at any given time only $N(t)$ are actually participating. Since the transition from the non-conductive to the conductive phase is thermally activated, it is logical to assume that the value of $N(t)$ should follow the rate law, as described in many common textbooks.[48,49] If the reaction is of first order, then the number of sites active in the conduction should have a time dependence of the form:

$$N(t) = N_0\left(1 - \exp(-kt)\right) \qquad 3.25$$

where t is the time since t_0, k is the rate coefficient, and N_0 is the number of sites. Substituting 3.25 into 3.24, we obtain:

$$\sigma(t) = \sigma_0 \exp\left(cN_0\left(1 - \exp(-kt)\right)^{1/3}\right) \qquad 3.26$$

To test this, and to even out the weighting of the data points, the time dependence of the sample's resistance *R(t)* was analyzed using the form:

$$\ln(R(t)) = d\left(1 - \exp(-k(t - t_0))\right)^{-1/3} \qquad 3.27$$

where d is the natural log of the final resistance at a given temperature, and t_0 is introduced to allow for the fact that it is not known exactly when the sample reached its final annealing temperature. Fits for this dependence are shown in Figure 3.11. The fits for the samples are on different plots because of the widely varying timescales of the annealing process.

It can be seen from Figure 3.11 that most of the fits are good, deviating only at higher temperatures. At the higher temperatures, the bulk of the annealing has taken place over a few minutes as opposed to hours or days at the lower temperatures. The resistance of the 5 wt% sample annealed at 198°C, which had the worst fit, changed by 5 orders of magnitude in 2 minutes. It is unlikely that the sample would have come into thermal equilibrium during this short time frame, so the actual temperature of the sample was probably non-uniform and time dependent.

The values of *d* and *k* that were obtained are shown in Table 3.2. It should be noted that *k* not only depends on the temperature, but also on the concentration of the graphene-based sheets in the sample.

Sample	*D*	k / hr $^{-1}$
0.5% 177C	10.7962 ± 0.0035	0.050656 ± 0.000087
0.5% 196C	9.9877 ± 0.0021	0.27503 ± 0.00041
0.5% 214C	9.8274 ± 0.0024	1.5253 ± 0.0042
0.5% 234C	9.188 ± 0.011	3.047 ± 0.035
0.5% 256C	8.6273 ± 0.0032	6.577 ± 0.045
0-75% 179C	10.6002 ± 0.0086	0.3196 ± 0.0017
0.75% 200C	9.559 ± 0.012	3.414 ± 0.053
0.75% 218C	8.7559 ± 0.0074	5.566 ± 0.068
0.75% 239C	8.138 ± 0.0046	11.40 ± 0.11
0.75% 258C	7.1530 ± 0.0060	10.96 ± 0.18
5% 156C	7.987 ± 0.010	3.175 ± 0.044
5% 180C	6.466 ± 0.039	5.96 ± 0.26
5% 198C	4.602 ± 0.076	4.54 ± 0.418

Table 3.2 Rate constants for the annealing of the composite samples

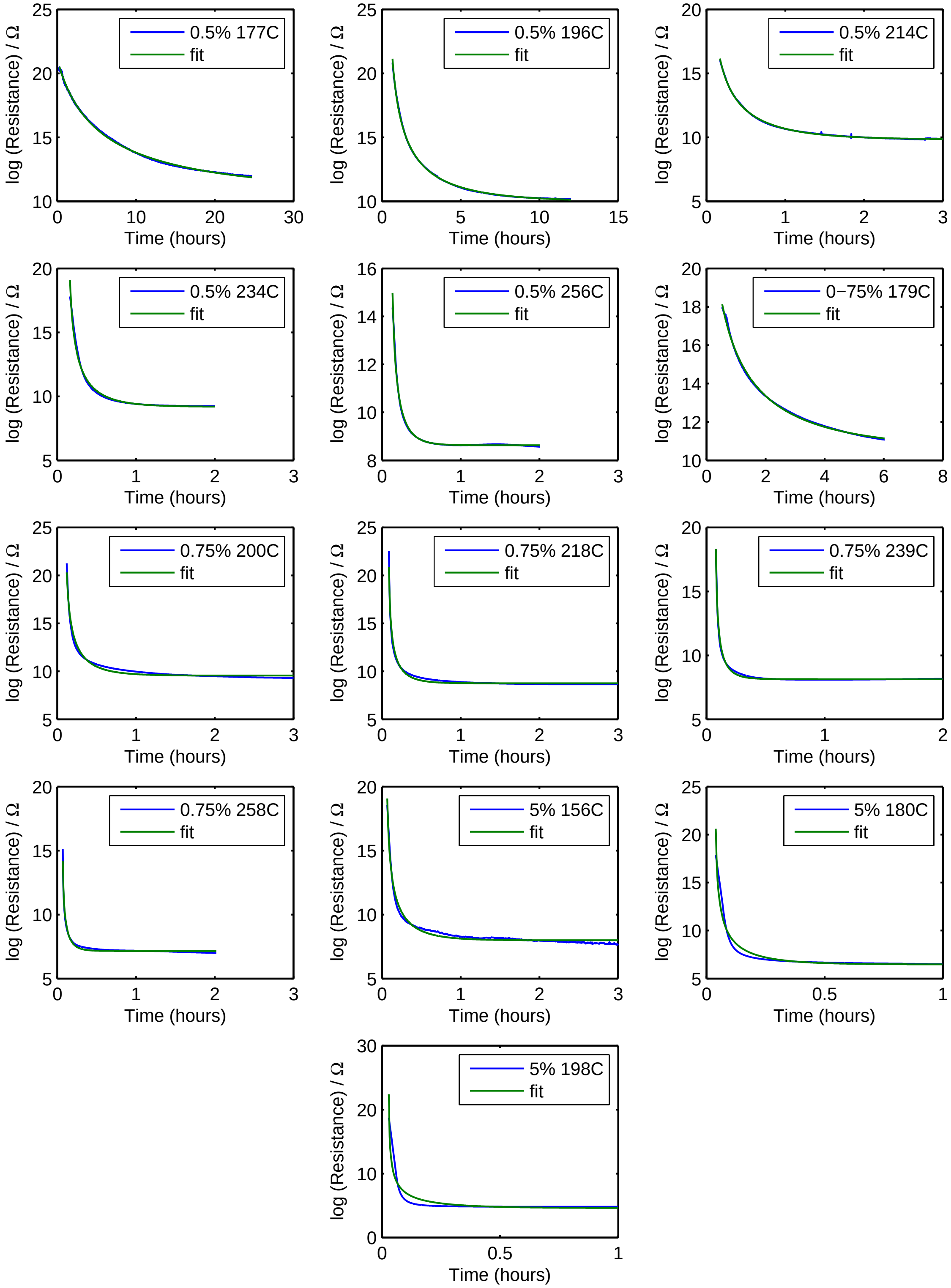

Figure 3.11 Resistance versus time as composite samples are annealed.

3.3.6. Activation energy of annealing

Since the annealing process is reversible and dependent on mechanical treatment, it seems unlikely that the conductivity change is due to a chemical change in the composite. It is therefore logical to assume that the change in conductivity might be due to a change in morphology in the composite.

Plots of ln(*k*) against 1/*T* for samples of the same concentration annealed at different temperatures are shown in Figure 3.12 For the 0.5wt% and 0.75wt% these plots have slopes of $(-1.477 \pm 0.55) \times 10^4\,\mathrm{K}$ and $(-1.18 \pm 0.83) \times 10^4\,\mathrm{K}$ respectively, giving an average of $(-1.33 \pm 0.54) \times 10^4\,\mathrm{K}$.

Taking the gas constant R to be $8.3145\mathrm{J\,K^{-1}}$ an Arrhenius analysis of Figure 3.12 yields an activation energy of:

$$(-1.33 \pm 0.54) \times 10^4\,\mathrm{K} \times 8.3145\mathrm{J\,K^{-1}} = 110.5 \pm 44.8\,\mathrm{kJ\,mol^{-1}}$$

Activation energy for the vacuous flow of polystyrene has been reported, but varies widely depending on the temperature and molecular weight of the polystyrene. At 200°C the activation energy of polystyrene of a molecular weight >25000 has been reported[50] to be $30\,\mathrm{kcal\,mol^{-1}} = 126\mathrm{kJ\,mol^{-1}}$, though in the same study the activation energy was reported to vary by a factor of 3 from this, depending on temperature and molecular weight. Other studies[51,52] have reported apparent activation energies in similar ranges. To test whether this apparent relaxation is related to the viscous flow of the polystyrene, the experiment could be repeated using composite materials made from polystyrene of different molecular weights, since viscosity of a polymer increases with molecular weight.

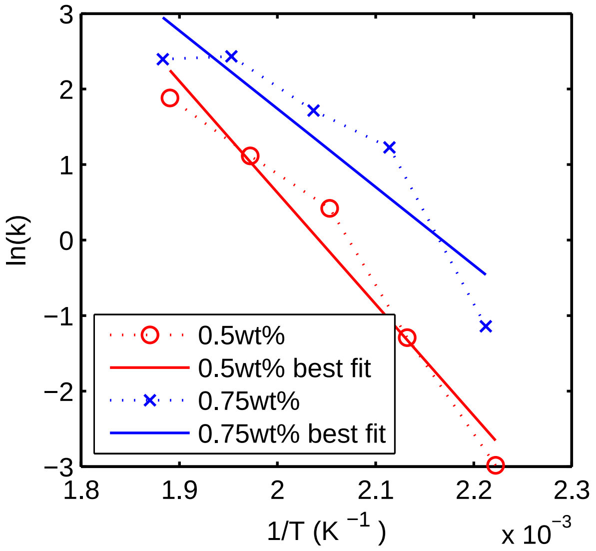

Figure 3.12 Arrhenius plots of the rate constants for the annealing of 0.5 % weight and 0.75% weight grapheene based filler composite materials.

4. Graphene-oxide Paper

Recently my group reported on the preparation and mechanical properties of a new material, graphene-oxide paper, formed by filtering a solution of exfoliated of graphite oxide[53]. Graphite oxide is produced by oxidation of graphite and consists of oxygenated graphene sheets (graphene oxide sheets) [54-56.] The latest structural models of graphite oxide postulates that the basal planes and edges of such sheets are decorated by oxygen-containing functional groups such as epoxide, hydroxyl, carbonyl, carboxyl.[57-60]. Due to the presence of these functional groups GO is hydrophilic and readily disperses in water. Previously we have demonstrated that ultrasonic treatment of aqueous dispersions of GO can result in its complete exfoliation, down to the level of individual graphene oxide sheets. [10,61] Vacuum or pressure-assisted filtration of such water dispersions results in the deposition of the graphene-oxide sheets and their assembly into macroscopic membranes (graphene-oxide paper). This material consists of graphene-oxide sheets stacked in a near parallel arrangement, thus forming a free-standing, paper-like membrane.

4.1. Chemical Properties of Graphene Paper

While graphene-oxide paper already possesses intriguing mechanical properties [53], it has potential to be further developed into a number of new materials that are of particular interest. Owing to the rich chemistry of oxygen-containing funtionalities in graphene oxide sheets,[60] their properties can be altered by chemical manipulation. In this way a number of new materials - functionalized graphene-oxide papers - with different mechanical, electrical and barrier properties can be accessed. For example, chemical deoxygenation (reduction) of such sheets can render them more graphene –like, and result in membranes that are electrically conductive (graphene paper).[61] Similarly, attachment of hydrophobic alkyl chains to the graphene-oxide sheets can alter their nature (from hydrophilic to hydrophobic) thus affecting the forces acting between the sheets and consequently, the mechanical properties of the paper.

In principal, one can envisage two potential routes for the preparation of such materials. The first approach, chemical modification of graphene-oxide sheets, would involve the preparation of functionalized graphite oxide, followed by exfoliation and reassembly by filtration. Indeed, in our previous work we have shown that certain chemically-modified graphite oxides can be completely exfoliated in organic solvents into functionalized graphene-oxide sheets, thus rendering this route a viable one[10]. This approach is not without drawbacks. In particular, the functionalized graphite oxide derivative must undergo sufficient exfoliation in a suitable solvent. This may not always be the case as some GO derivatives do not exfoliate at all. One clear example is the electrically-conductive reduced graphene-oxide sheets as discussed in chapter 3 of this work. Assembly of such sheets, exfoliated at the individual level, would afford electrically conductive graphene-based membranes. However, the reduced sheets are hydrophobic, and tend to strongly aggregate and agglomerate[61], which makes preparation of their dispersions, and thus assembly into macrostructures, impossible. The drawback of the above method is that the complete exfoliation of functionalized graphite oxides into individual sheets typically requires large volumes of organic solvents.

It was observed that samples of graphene oxide paper, when exposed to water or organic solvents, would swell. Such swollen papers would lose their mechanical integrity and disintegrate if not handled carefully. However, it was found that after drying, mechanical integrity was restored, and the morphology unchanged.[53] Therefore, even though graphene-oxide paper consists of tightly-packed graphene oxide sheets, solvent molecules can readily penetrate between the sheets, while not disturbing the overall morphology of the sample. With this in mind, one can envisage a second approach, where molecules which react with the graphene-oxide sheets can also penetrate the assembly, react with the sheets, and thus furnish functionalized derivatives of graphene oxide paper. In this work we demonstrate the viability of this approach.

4.2. Chemical modification of Graphene-based paper

To examine the feasibility of the post-synthetic modification approach we selected a well-known reaction of graphite oxide with amines.[62-64] It has been demonstrated in the literature that primary alkylamines can easily react with graphite oxide and often form well-defined derivatives. Furthermore, such reactions lead to intercalation of amine molecules between the graphene oxide sheets in GO thus resulting in a predictable increase in the spacing between the graphene-oxide sheets. Given that in graphene-oxide paper the ordered arrangement of graphene-oxide sheets results in the appearance of a diffraction signature, such features allow for the reactions between graphene-oxide paper and alkylamines to be studied by X-ray diffraction.

GO prepared by the Hummers method is discussed in section 3.1. Graphene oxide paper was prepared by pressure-assisted filtration of aqueous dispersions of exfoliated GO (3 mg/mL) through polycarbonate filters (Isopore Membrane Filters, 200 nm pore size, Millipore) using Fisherbrand Pressure Holder with 1.5 L reservoir, with an air pressure of 30 psi. Following filtration of the aqueous dispersions and membrane drying, the membrane filter was removed by dissolving it in a minimal amount of methylene chloride. Samples of graphene-oxide paper (1 x 2 cm) were cut and subsequently soaked in methanol solutions of various alkyl amines (0.1 M), at room temperature for 24 hours. Following the reaction, the samples were either briefly rinsed with pure methanol (5 minutes), or soaked in the same solvent for another 24 hours, dried and analyzed further.

The first indication that the amine molecules were indeed able to penetrate graphene-oxide paper, and remain in it even after rinsing with pure solvent comes from the recorded mass increase in the samples (before and after the amine treatment). Mass increases of 6.6, 13.9, and 38.6 % were recorded for the samples treated with butyl-, octyl-, and dodecylamine, respectively. Similarly, elemental analyses (Atlantic Microlab, Norcross, GA) of the intercalated paper samples (nitrogen content) revealed that there was one amine molecule intercalated for every 17.8, 15.9, and 13.9 graphene carbons for butyl-, octyl-, and dodecylamine, respectively. Based on this analysis it appears that a greater mass of amine molecules was intercalated for the longer-alkyl-chain amines. This can be explained by physical intercalation of the long-alkyl-chain amines. Due to the hydrophobic nature of their alkyl chains, and their size, the larger molecules were more difficult to rinse out of the layered paper structure.

4.2.1. X-Ray Analysis of Graphene Based Paper

To measure the spacing of the sheets in the paper, X-ray diffraction was performed using a Rigaku ATXG. A holder was made so that the paper was mounted by its ends in such a way that there was nothing within 3mm behind the paper. This was desirable since the paper is only a few 100’s of μm thick, and carbon has a low X-ray cross section. If the paper had been mounted on a substrate, it would have been essential to use a substrate with a very low X-ray scattering cross section. The paper was aligned to the beam by first quickly scanning the sample to find the approximate angle at which the peak was, then maximizing the signal scanning the sample through its two rotation angles. This method was chosen in preference to aligning the surface of the sample at a small reflection angle because the graphene-based platelets were very often out of alignment with the plane of the paper that they were forming by up to 5º. Whichever method of aligning the samples was used had very little effect on the measured spacing, but did affect the magnitude of the X-ray signal that was collected.

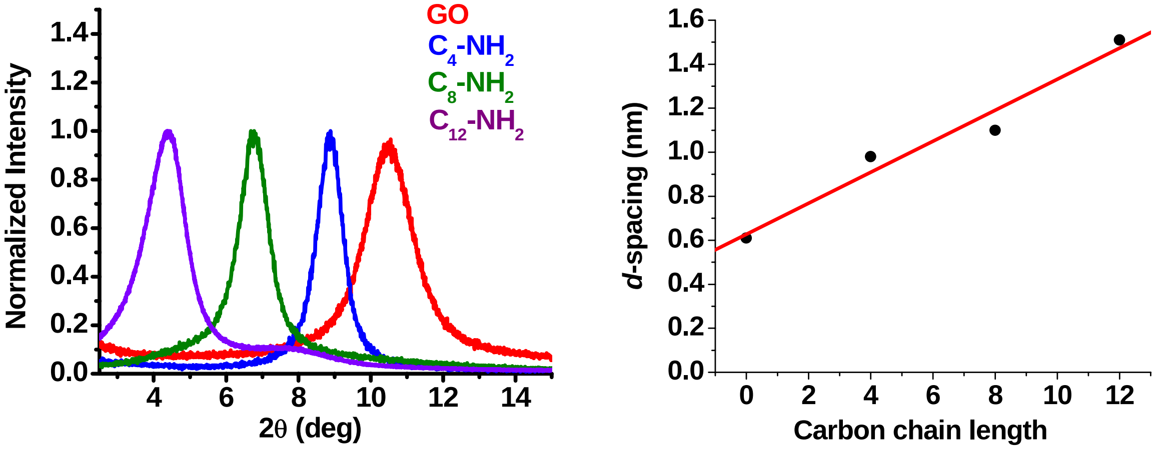

Figure 4.1 X-Ray diffraction patterns of pristine and amine-treated samples of graphene oxide paper (left). Dependence of the d-spacing on the alkyl chain length (right).

While pristine graphene-oxide paper displays an X-ray diffraction peak typically at 0.83 nm (this value is dependent on the method of preparation and on the humidity level), in the amine-treated samples the position of this signal was shifted to higher values, depending on the length of the amine alkyl chain, and on the rinsing protocol. More importantly, in all amine-treated samples, only one diffraction peak was observed, clearly indicating that penetration of the amine into the paper sample and the reaction were complete as shown in Figure 4.1. For the graphene-oxide-paper sample treated with butyl-, octyl- and dodecylamine and subjected to a brief methanol rinse, the recorded d-spacings were 1.00, 1.30, and 2.01 nm respectively. Following the 24-hour soaking in methanol, the measured d-spacings decreased to 9.83, 1.10and 1.51 nm respectively, and did not change upon further exposure to methanol. These values are close to those reported in the literature for GO intercalated with the same alkyl amines.[65] As noted above, along with the results of elemental analyses, this indicates that brief rinsing with methanol does not remove all amine molecules that are physically intercalated between the graphene-oxide layers. Surprisingly however, it appears that both the physically-intercalated and chemically-bound amine molecules are ordered between the graphene-oxide sheets, thus resulting in paper materials with fairly well defined intersheet spacing. If the measured d-spacings are plotted against the number of carbon atoms in the alkylamine, a fairly good linear fit is obtained (Figure 4.1, right). Note that the value used for pristine GO paper itself is 0.61 nm, which is the value reported for "dry" graphite oxide, that is, GO which is intercalated with the minimal amount of water possible.

Scanning electron microscopy (SEM) images of the fracture surfaces of the amine-treated samples revealed that, upon reaction with amines, such samples become visibly thicker, which is in accord with the increased inter-sheet distance. For example (Figure 2), a ~10μm thick sample of graphene-oxide paper increased in thickness to ~25μm upon exposure to dodecylamine and a brief methanol rinse. Such increase in thickness also corresponds roughly to the recorded increase in d-spacing for this particular sample (from 0.83 nm to 2.01 nm). More importantly, the SEM imaging revealed that the morphology of the amine-treated samples was not altered by the treatment, and that the near parallel arraignment of the stacked graphene-oxide sheets was maintained in the paper samples.

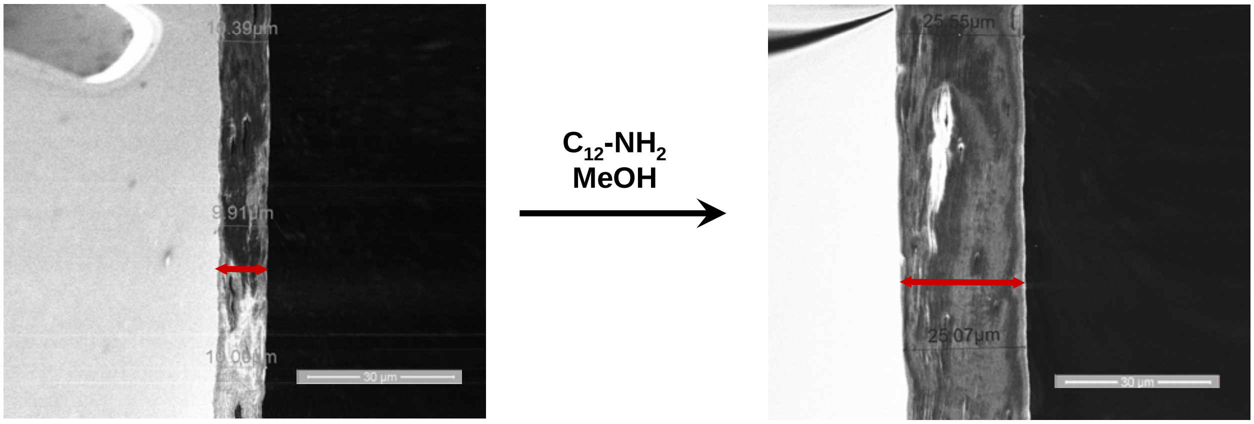

Figure 4.2 SEM images of the fracture surface of a ~10 mm-thick graphene oxide paper sample before and after treatment with dodecylamine.

In conclusion, it has been successfully demonstrated that preparation of modified graphene-oxide papers via post assembly modification is a viable route, which will allow a number of macrostructured graphene-based materials with different properties to be accessed.

5. Summary and Future Work

2D nanostructures are attractive because of their novel mechanical, electronic and physical properties, and potential applications in nano-electronics and nano-composites. Techniques for synthesizing bulk amounts of these structures are therefore an important research topic.

In this thesis, progress has been made on understanding graphene-based structures in nano-composites, and the importance of understanding the polymer as well as the nanostructure has been shown. Accomplishments have also been made on developing methods for measuring very high input impedances using a standard cryostat. It has also been successfully demonstrated that preparation of modified graphene-oxide papers via post assembly modification is a viable route.

Future research could take a variety or directions. The most important direction would be to investigate the nano-composites made with purified graphene-based sheets, and with sheets exfoliated by stirring rather than ultrasonication. As described in section 3, the exfoliated platelets do contain salts, and it is known that exfoliation by stirring results in much larger sheets than those studied in this work. Attempts to purify the sheets have so far have attempted to use dialysis; however the standard cellulose dialysis tubes are not completely stable, and have so far resulted in adding more contamination than they are able to take away. Purification using a porous alumina membrane would be another approach that could be tried, as this would be stable at high temperatures, and can be baked to remove contaminants if necessary.

Better understanding of the interaction between the polymer and the sheets and any other materials present would be of great interest. The flow of the polymer greatly affects the conductivity of the composite. If the application of the hopping model to this composite is correct (it fits the data very well), it makes little sense for the gain in conductivity to be attributed to a simple percolation problem. The mechanism of conduction has been shown to be a hopping model, which requires the conduction electrons to be weakly bound to states that are spatially isolated. It is therefore more likely that there is some kind of interaction that enables sites within the material to act as electron donors. It was also found that if the composite powder was not vacuum dried sufficiently thoroughly, the conductivity could be killed. The origin of this interaction should be investigated. A starting point for this would be to test whether the rate at which the composites regain their conductivity as they are annealed depends on the molecular weight of the polymer or not.

References

1 Novoselov K.S.; Geim A.K.; Morozov S.V.; Jiang D.; Zhang Y.; Dubonos S.V.; Grigorivea I.V.; Firsov A.A. *Science*, **2004**, 306, 666.

2 Novoselov K.S.; Geim A.K.; Morozov S.V.; Jiang D.; Zhang Y.; Katsnelson I.V.; Grigorivea I.V.; Dubonos S.V.; Firsov A.A. *Nature*, **2005**, 438, 197.

3 Zhang Y.; Tan Y.; Stomer H.L.; Kim P. *Nature*, **2005** 438, 201.

4 Zhang Y.; Small J.P.; Amori M.E.S.; Kim P.; *Phys. Rev. Lett*. **2005**, 94, 176803.

5 Berger C.; Song Z.; Tianbo L.; Li X.; Asmerom Y.; Ogbazghi; Feng R.; Dai Z.; Marchenkov A.N.; Conrad E.H.; First P.N.; de Heer W.A. *J. Phys. Chem. B*, **2004**, 108, 19912.

6 B.I. Bleaney, B.B. Electricity and Magnetism. *Oxford University Press* 2nd edn Vol. 2nd Edition (London, 1964).

7 Hyun, S., Thorpe, M.F., Jaeger, M.D., Golding, B. & Day, A.R. Resistivity determination from small crystallites. *Physical Review B* 57, 6697 (1998).

8. Zimney E.J.; Dommett G.H.B; Ruoff R.S.; Dikin D.A. Northwestern University, Evanston, IL Correction factors for 4-probe electrical measurements with finite size electrodes and material anisotropy: a finite element study Unpublished.

9 Adriaanse L,J,; Faneyte I-P.; Martens H.C.F.; Reedijk J.A.; Brom H.B.; Michels M.A.J.; Brokken_Zijp J.C.M *Synthetic Metals,* **1997,** 84, 871.

10 Stankovich S.; Dikin D.A.; Dommett G.H.B. *Nature*, **2006**, 442, 282.

11 Mandal P.; Neumann A.; Jansen A. G. M.; Wyder P. *Physical Review B*, **1997** 55, 452.

12 Mehbod M.; Wyder P.; Deltour R.; Pierre C.; Geuskens, G. *Physical Review B*, **1987**, 36, 7627.

13 Quivy A.; Deltour R.; Jansen A.G.; Wyder P. *Physical Review B*. **1989**, 39, 1026.

14 Medalia A.I. *Rubber Chemistry and Technology*, **1986,** 59, 432.

15 Sichel E.K.; Gittleman J.I.; Sheng P. *Physical Review B*, **1978,** 18, 5712.

16 Huang J. *Advances in Polymer Technology*, **2002,** 21. 299.

17 Reidy R.F.; Simkovich G. *Journal of Materials Science* **1993**, 28, 799.

18 Sherman R.D.; Middleman L.M.; Jacobs, S.M.; *Polymer Engineering and Science* **1983,** 23, 36.

19 Sichel E.K.; Gittleman J.I.; and Sheng, P. *Journal of Electronic Materials* **1982,** 11, 699.

20 Sheng, P.; Sichel, E.K.; Gittleman, J.I. *Physical Review Letters* **1978**, 40, 1197.

21 Kirkpatric S. *Reviews of Modern Physics* **1973,** 45, 574.

22 Carmona F. *Physica A* **1999**, 157, 461.

23 Dawson, J.C.; Adkins C.J. *J. Phys. Condensed Matter* **1996,** 8, 8321.

24 Connor M.T.; Roy S.; Ezquerra, T.A.; Baltá Calleja F.J. *Physical Review B*.**1998,** 57, 2286.

25 Mott N.F. *J. Non-Crystal. Solids* **1968**, 1, 1.

26 Mott N. F. *Philos. Mag.* **1969**, 19, 835.

27 Halperin B. I.; Langer J. S. *Physical Review B*, **1971,** 4, 2612.

28 Shklovskii B.I.; Efros A.L. *Electronic Properties of Doped Semiconductors*; Springer, Berlin, **1984**.

29 Miller A.; Abrahams E. *Phys. Rev.* **1960**. 120, 745.

30 Ambegokar, V.; Halperin B.I.; Langer J.S. *Phys Rev B* **1971**, 4, 2612.

31 Skal A.S.; Shklovskii B.I. *Sov. Phys,-Solid State* **1971**, 16, 1190.

32 Pollak M. *J. Non-Crystal. Solids* **1972**, 11, 1.

33 Hamilton E.M. *Phil. Mag.* **1972**. 26, 1043.

34 Tchoudakov R.; Narkis M.; Siegmann A. *Polymer Engineering and Science*, **2004**, 44, 528.

35 Flow Kills Conductivity of Single Wall Carbon Nanotubes (SWNT) Composites URL. http://meetings.aps.org/link/BAPS.2006.MAR.V25.2

36 Van Der Putten, D.; Monen J. T.; Brom, H. B.; Brokken-Zijp, J. C. M.; Michels M. A. *J.Synthetic Metals*, **1993,** 55-57, 5057.

37 L. J. Adriaanse, I.-P. Faneyte, H. C. F. Martens, J. A. Reedijk, H. B. Brom, J. C. M. Michels, and J. C. M. Brokken-Zijp, Synthetic Metals, Vol.84, pp871-872 (1997).

38 Chandrasekhar P. *Conductive Polymers Fundamentals and Applications*, , Kluwer Academic Publishers, **1999**

39 Adriaanse L. J.;. Brom H. B.; Michels M. A.; Brokken-Zijp J. C. M *.Physical Review B*, **1997,** 55, 9383.

40 Shklovskii B.I.; Efros A.L. *Electronic Properties of Doped Semiconductors*; Springer, Berlin, **1984**.

41 Gaál R.; Salvetat J.P.; Forro L. *Phys. Rev. B* **2000** 61, 7320.

42 Yosida Y.; Oguro I. *J. Appl. Phys*. **1999**, 86, 999.

43 Yosida Y.; Oguro I. *J. Appl. Phys*. **1998**, 83, 498.

44 Fuhrer M.S.; Holmes W.; Richards P.L.; Delaney P.; Louie S.G.; Zettl A. *Synthetic Metals* **1999**, 103, 2529.

45 Shibayama Y.; Sato H.; Enoki T.; Bi X.; Dresselhaus M.; Endo M. *Journal of the Physical society of Japan* **2000**, 69, 754.

46 Shekhar S.; Prasad V.; Subramanyam S.V. *Physics Letters A* **2006**, 360, 390.

47 Benoit J.M.; Corraze B.; Chauvet O. *Phys. Rev. B* **2002**, 65, 241405(R)

48 Atkins P.W. *Physical Chemistry* Oxford University Press, Oxford **1998**

49 Sperling L.H. *Introduction to Physical Polymer Science* John Wiley & Sons inc. New York **1992**

50 Fox T.G.; Flory P.J. *Journal of Polymer Science Part B* **1996**, 34,207.

51 Patel M. *Polymer Testing* **2004**, 23, 107.

52 Karam H.J.; Bellinger J.C. *Transactions of the society of Rheology* **1969**, 13, 209.

53 Dikin D.A.; Stankovich S.; Zimney E.J.; Piner R.D.; Dommett G.H.B.; Evmenenko G.; et al. Preparation and characterization of graphene oxide paper. *Nature* **2007**; submitted.

54 Brodie B.C.; *Ann Chim Phys* **1860**;59, 466.

55 Hummers W,; Offeman R. *J Am Chem Soc* **1958**, 80, 1339.

56 Staudenmaier L. *Ber Dtsch Chem Ges* **1898**, 31, 1481.

57 He H.; Klinowski J.; Forster M.; Lerf A. *Chem Phys Lett* **1998**; 287, 53.

58 He H.; Riedl T.; Lerf A.; Klinowski J. S. *J Phys Chem* **1996**;100, 19954.

59 Lerf A.; He H.; Forster M.; Klinowski J. *J Phys Chem B* **1998**;102, 4477.

60 Lerf A.; He H.; Riedl T.; Forster M.; Klinowski J. *Solid State Ionics* **1997**; 101-103(Pt. 2), 857.

61 Stankovich S.; Dikin D.A.; Piner R.D.; Kohlhaas K.A.; Nguyen S.T.; Ruoff R.S. Synthesis of graphene-based nanosheets via chemical reduction of exfoliated graphite oxide. *Carbon* **2007**;in press.

62 Bourlinos AB.; Gournis D.; Petridis D.; Szabo T.; Szeri A.; Dekany I. *Langmuir* **2003**, 19, 6050.

63 Matsuo Y.; Miyabe T.; Fukutsuka T.; Sugie Y.; *Carbon* **2007**, 45, 1005

64 Nethravathi C.; Rajamathi M. *Carbon* **2006**, 44, 2635.

65 Nethravathi C.; Rajamathi M. *Carbon* **2006**, 44, 2635.